Morphogen gradient orchestrates pattern-preserving tissue morphogenesis via motility-driven unjamming
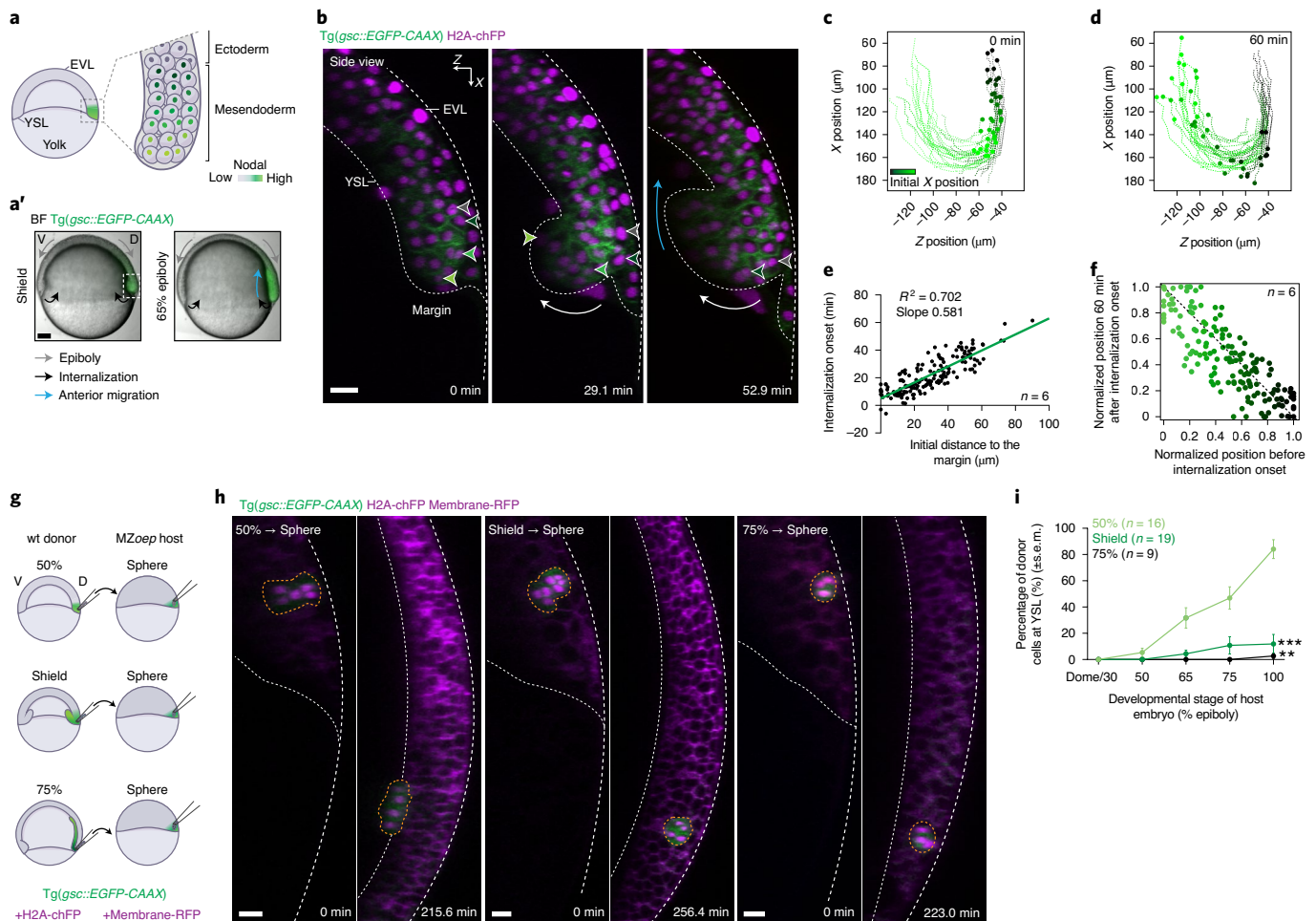
Diana Pinheiro, Roland Kardos, Édouard Hannezo ⬤ ✉ and
Carl-Philipp Heisenberg ⬤ ✉

Embryo development requires biochemical signalling to generate patterns of cell fates and active mechanical forces to drive tissue shape changes. However, how these processes are coordinated, and how tissue patterning is preserved despite the cellular flows occurring during morphogenesis, remains poorly understood. Gastrulation is a crucial embryonic stage that involves both patterning and internalization of the mesendoderm germ layer tissue. Here we show that, in zebrafish embryos, a gradient in Nodal signalling orchestrates pattern-preserving internalization movements by triggering a motility-driven unjamming transition. In addition to its role as a morphogen determining embryo patterning, graded Nodal signalling mechanically subdivides the mesendoderm into a small fraction of highly protrusive leader cells, able to autonomously internalize via local unjamming, and less protrusive followers, which need to be pulled inwards by the leaders. The Nodal gradient further enforces a code of preferential adhesion coupling leaders to their immediate followers, resulting in a collective and ordered mode of internalization that preserves mesendoderm patterning. Integrating this dual mechanical role of Nodal signalling into minimal active particle simulations quantitatively predicts both physiological and experimentally perturbed internalization movements. This provides a quantitative framework for how a morphogen-encoded unjamming transition can bidirectionally couple tissue mechanics with patterning during complex three-dimensional morphogenesis.

Embryogenesis involves precise and highly reproducible cell and tissue movements, which shape the embryo and position the newly specified progenitor cells along the future body axes. Experimental and theoretical work over the last decades has provided insight into the molecular signals and gene regulatory networks involved in tissue patterning. Many of these signals were shown to function as morphogens, diffusible molecules which form signalling gradients within tissues and induce cell fate in a concentration-dependent manner[1]. Likewise, considerable progress has been made in understanding the cellular processes and active mechanical forces involved in sculpting tissues and embryos[2–7]. In contrast, the mechanochemical mechanisms coordinating tissue patterning and morphogenesis remain poorly understood.

Gastrulation is an excellent model to address this question, as it constitutes the first major morphogenetic event in development during which the germ layers (ectoderm, mesoderm and endoderm) are both specified and shaped. During zebrafish gastrulation, highly conserved Nodal morphogens, members of the transforming growth factor-β family, form a signalling gradient at the blastoderm margin and

Institute of Science and Technology Austria, Klosterneuburg, Austria. ✉e-mail: edouard.hannezo@ist.ac.at; heisenberg@ist.ac.at

Fig. 1 | The internalization capacity of mesendoderm cells decays rapidly during gastrulation. a,a′, Schematic representation of mesendoderm patterning (**a**) and morphogenesis (**a′**) during zebrafish gastrulation. Nodal signalling gradient is colour coded in green (**a**). Bright-field (BF) single-plane images of a gastrulating embryo expressing *gsc::EGFP-CAAX*, to mark the axial mesendoderm (**a′**). Arrows highlight morphogenetic movements. White dashed box indicates the embryo dorsal side. **b**, High-resolution confocal images of axial mesendoderm internalization, marked by *gsc::EGFP-CAAX* expression (green), in a wt embryo. H2A-chFP (magenta) marks all cell nuclei. Dashed lines indicate the enveloping layer (EVL) and yolk syncytial layer (YSL). Arrows as in **a′**. Arrowheads indicate the position of four cells during internalization. Internalization onset is at 0 min. **c,d**, Individual tracks of the mesendoderm cells shown in **b** at internalization onset (**c**) and 60 min later (**d**). Colour code corresponds to the initial distance of internalizing cells to the blastoderm margin. **e**, Onset of mesendoderm cell internalization as a function of their initial distance to the blastoderm margin in wt embryos (*N* = 6). **f**, Correlation between mesendoderm cell position pre- and post-internalization in wt

embryos (*R*² = 0.63, *N* = 6; Supplementary Note). Dashed line indicates perfect conservation of the relative cell position during internalization (*R*² = 1). Colour code as in **c** and **d**. **g,h**, Schematic representation of the heterochronic transplants (**g**) shown in high-resolution confocal images of transplanted mesendoderm donor cells (**h**), collected from the dorsal blastoderm margin of 50%, shield and 75% epiboly stage embryos. Donor cells are marked by *gsc::EGFP-CAAX* (green) and H2A-chFP expression (magenta, nuclei). MZ*oep* hosts express low levels of *gsc::EGFP-CAAX* (green) and Membrane-RFP (magenta). For each transplant, the first time point (0 min) and the time point when hosts reached 100% epiboly are shown. Dashed white lines as in **b**. Dashed yellow lines highlight the donor cell transplants. **i**, Percentage of donor mesendoderm cells, collected from 50% (*N* = 9), shield (*N* = 12) or 75% epiboly (*N* = 8) stage embryos, located at the YSL as a function of the host developmental stage. Data shown as mean ± s.e.m. Kruskal–Wallis test. ***P = 0.0001, **P = 0.0010 (**i**). Lateral view in **a**. Dorsal view (cross-section in **b** and **h**). D: dorsal; V: ventral in **a′, g**. Scale bars: 100 μm (**a**) and 20 μm (**b** and **h**).

induce mesoderm and endoderm (mesendoderm) cell fate specification in a dose-dependent manner (Fig. 1a)[8–11]. Since Nodal signals act primarily before gastrulation[12], mesendoderm specification is largely completed before or concomitant with the onset of its internalization movements beneath the ectodermal layer[2,10]. Interestingly, while in multiple organisms mesendoderm internalization involves various degrees of epithelial-to-mesenchymal transitions and large-scale cellular flows, the relative position of mesendoderm progenitors before internalization is still indicative of their ultimate fate and position after gastrulation[2,10,13,14]. Yet, how such positional information is preserved during the complex three-dimensional (3D) flows associated with gastrulation remains unclear.

Mesendoderm internalization is thought to be a cell-autonomous process with cells actively ingressing as individuals[2,15–17]. Differential tissue surface tension, based on differences in cell–cell adhesion and cortical tension, was originally proposed to dynamically regulate mesendoderm internalization[18–21]. More recent studies, however, suggested that these differences might not be sufficient to drive mesendoderm cell internalization in vivo, and that this involves directed single-cell migration[22–25]. Yet, it is unclear how to relate such individual internalization capacity to the highly synchronized movements observed in vivo[17,26,27]. Theoretical studies, supported by work on cell monolayers, suggested that the interplay between single-cell migration forces and supra-cellular mechanical interactions can trigger changes in

collective cell behaviour resembling jamming and glass transitions previously described for passive systems[28–30]. This raises questions as to the relative contributions of single-cell mechanics, compared with collective and emergent tissue properties, to mesendoderm internalization in vivo.

Internalization capacity of mesendoderm cells decays abruptly during gastrulation

To address how mesendoderm patterning is preserved during gastrulation, we first tracked the individual movements of dorsal mesendoderm progenitors during internalization and subsequent anterior migration (Fig. 1a′ and Extended Data Fig. 1a). In line with previous work[17,26,27], we observed that mesendoderm internalization was spatially restricted to the blastoderm margin (Fig. 1b–d and Supplementary Video 1). Moreover, the timing of cell internalization was closely correlated with the initial distance to the margin, with cells further away internalizing later than cells right at the margin (Fig. 1e, Extended Data Fig. 1b and Supplementary Video 1). This tight link between the position and timing of cell internalization thus ensures that the first mesendoderm cells to undergo internalization will also be the first to migrate away from the margin, thereby preserving positional information between pre- and post-internalizing progenitors ($R^2 = 0.63$; Fig. 1f).

An intuitive model for linking position to internalization timing would be that the dynamics of mesendoderm cell internalization are set by an intrinsic timer[31]. To test this, we designed a set of heterochronic transplantations where mesendoderm progenitors, collected from the dorsal blastoderm margin of wild-type (wt) donor embryos at different stages of gastrulation, were transplanted into the superficial layers of the blastoderm of sphere stage maternal-zygotic *oep* mutant (MZ*oep*) host embryos, which lack most mesendoderm progenitors and internalization movements[26,32] (Fig. 1g and Extended Data Fig. 1a). With this, the autonomous migratory capacity of the donor cells can be distinguished from collective effects arising during normal gastrulation movements. Given that all mesendoderm donor cells were collected at the time and position where they internalize in vivo (that is, the blastoderm margin), all cells would thus be expected to internalize with similar dynamics according to the timer hypothesis. In striking contrast, however, we found that only mesendoderm cells collected from early donor embryos (50% epiboly stage) efficiently internalized by the end of host embryo gastrulation (Fig. 1h,i, Extended Data Fig. 1c and Supplementary Video 2). Cells collected from donor embryos at later stages of gastrulation (shield and 75% epiboly stages), however, failed to undergo internalization and, instead, remained in superficial positions within the blastoderm (Fig. 1h,i, Extended Data Fig. 1d,e and Supplementary Video 2). Importantly, this abrupt loss of internalization competence of mesendoderm cells appeared to be (i) cell-autonomous, as it was independent of the initial number of transplanted cells (Extended Data Fig. 1f), the initial distance of the transplanted cells to the host margin (Extended Data Fig. 1f′) or the developmental mismatch between donors and hosts (Extended Data Fig. 1g–i) and (ii) similar along the blastoderm margin, as assessed by transplantation of ventral progenitors at different stages of gastrulation (Extended Data Fig. 1j–l). Altogether, these findings argue for a window of competence for autonomous mesendoderm cell internalization that is closed by mid-to-late shield stage, well before the completion of internalization movements at the tissue scale. This contrasts with the view that zebrafish mesendoderm progenitors internalize simply via autonomous and synchronized ingression of single cells[15–17] and suggests that collective properties might be involved.

A progressive decrease in mesendoderm cell protrusiveness underlies the temporal switch of internalization capacity

To elucidate the cellular and biophysical basis for the rapid loss of autonomous internalization competence, we transplanted small clusters of F-actin-labelled mesendoderm progenitors from donor embryos at different stages of gastrulation and systematically analysed their protrusive activity in 3D over time (Methods). We reasoned that the rapid loss of autonomous internalization capacity in late mesendoderm cells could be due to a loss of cell polarization towards the yolk syncytial layer (YSL) and/or decreasing motility forces, eventually rendering these cells unable to drive the local cell–cell rearrangements necessary for internalization. While cell protrusions were still preferentially directed to the YSL in late internalization-incompetent progenitors (Fig. 2a and Extended Data Fig. 2a), we found that both the number and length of their cellular protrusions were on average lower than those of early internalization-competent cells (Fig. 2a–c and Extended Data Fig. 2b–e). This suggests that the loss of internalization competence in late mesendoderm cells might result from decreasing protrusiveness, rather than from a loss of cell polarization.

We thus reasoned that a critical value of protrusive/motility forces might be necessary to drive the cell–cell rearrangements necessary for mesendoderm cell internalization, reminiscent of the theoretically proposed phenomenon termed 'motility-driven (un) jamming'[33]. To test this, we first compared the mean squared relative displacement (MSD), a critical parameter to distinguish jammed from unjammed states, between mesendoderm progenitors transplanted from early (50% epiboly) and late donor embryos (shield and 75% epiboly). In line with the notion that internalization-competent and internalization-incompetent mesendoderm progenitors are above or below the critical motility forces, respectively, we found that, in contrast to early progenitors, late cells displayed strongly caged motion, with limited rearrangements even over time scales of several hours (Extended Data Fig. 2f,g and Supplementary Video 3). To directly test the link between cell protrusiveness and internalization capacity, we expressed low levels of a dominant-negative version of Rac1 (DN-Rac1), a GTPase implicated in regulating mesendoderm motility[23,24,34], in internalization-competent early cells. Interestingly, even a mild reduction of the average number and length of protrusions in DN-Rac1-overexpressing early cells (Fig. 2a,b and Extended Data Fig. 2a,e) was sufficient to drastically reduce their internalization competence (Fig. 2c and Extended Data Fig. 2h–j′). This indicates that the degree of protrusion formation is critical for the internalization competence of mesendoderm cells, and further suggests that reducing the motility forces of mesendoderm progenitors below a critical value is sufficient to jam these cells.

Nodal signalling regulates mesendoderm cell protrusiveness and internalization capacity via a motility-driven (un) jamming transition

Next, we asked how this temporal change in mesendoderm protrusiveness, and thus internalization competence, is regulated molecularly. Since Nodal signalling was previously implicated in regulating mesendoderm internalization[15,16,25,32], we reasoned that changes in Nodal signalling levels might be involved. In line with previous observations[35–39], we found that nuclear accumulation of phosphorylated Smad2/3 complexes (pSmad2/3), a proxy for Nodal signalling activation[8–11], was highest at the blastoderm margin of embryos at the onset of gastrulation (50% epiboly; Fig. 2d and Extended Data Fig. 2k). Notably, peak levels of nuclear pSmad2/3 in pre-internalizing progenitors decreased at later stages of gastrulation (shield and 75% epiboly; Fig. 2d and Extended Data Fig. 2k).

To directly test whether these temporal changes in morphogen signalling might function as a control parameter tuning mesendoderm protrusiveness, and thus internalization competence, we uniformly overexpressed Nodal ligands (Extended Data Fig. 3a,b)[20] and transplanted these progenitors from shield stage donor embryos into MZ*oep* hosts. Overexpressing cells exhibited not only homogeneously higher Nodal signalling (Extended Data Fig. 3c–f) but also a mild increase in the average number and length of their cellular protrusions (Fig. 2e,f and Extended Data Fig. 3l,m). Consistent with the idea that a critical
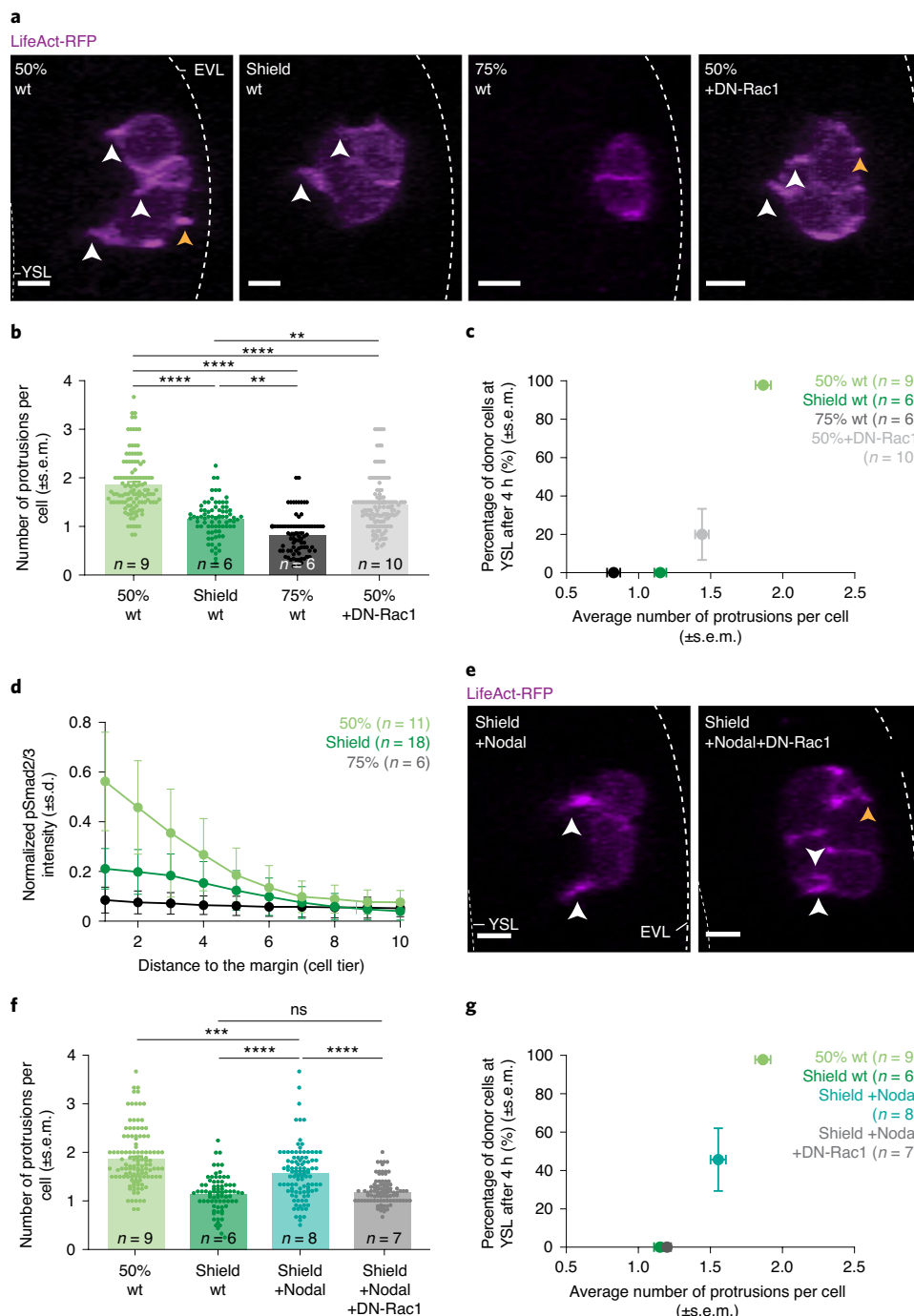
Fig. 2 | Nodal signalling regulates mesendoderm cell protrusiveness and internalization capacity. a, High-resolution confocal images of transplanted wt or DN-Rac1-overexpressing donor mesendoderm cells, collected from 50%, shield or 75% epiboly stage embryos. Donor cells are marked by *gsc::EGFP-CAAX* (not shown) and LifeAct-RFP expression (magenta). Dashed lines indicate the EVL and YSL. Arrowheads indicate cell protrusions oriented towards the YSL (white) or EVL (yellow). **b**, Average number of protrusions formed per wt or DN-Rac1-overexpressing mesendoderm donor cell, collected from 50% (wt: 44 cells, *N* = 7; +DN-Rac1: 54 cells, *N* = 10), shield (wt: 36 cells, *N* = 4) or 75% epiboly (wt: 26 cells, *N* = 5) stage embryos, upon transplantation (see also Extended Data Fig. 2b–d). **c**, Percentage of internalized wt or DN-Rac1-overexpressing mesendoderm donor cells, collected from 50%, shield or 75% epiboly stage embryos, as a function of their average number of protrusions (see **b** for *n* and *N*). **d**, Normalized intensity of nuclear pSmad2/3 as a function of the distance to the blastoderm margin in wt embryos at 50% (*N* = 5), shield (*N* = 6) and 75% epiboly (*N* = 3) stage (see also Extended Data Fig. 2k). **e**, High-resolution confocal images

of transplanted mesendoderm donor cells overexpressing Nodal, alone or in combination with DN-Rac1, collected from shield stage embryos. Donor cells, dashed lines and arrowheads as in **a**. **f**, Average number of protrusions formed per wt or Nodal-overexpressing mesendoderm donor cell, collected from control and DN-Rac1 expressing embryos at 50% epiboly (wt: 44 cells, *N* = 7) or shield stage (wt: 36 cells, *N* = 4; +Nodal: 47 cells, *N* = 5; +Nodal+DN-Rac1: 48 cells, *N* = 7), upon transplantation (wt data also shown in **b**). **g**, Percentage of internalized wt and mesendoderm donor cells overexpressing Nodal, alone or in combination with DN-Rac1, collected from 50% epiboly- or shield stage embryos, as a function of their average number (see **f** for *n* and *N*). In **b** and **f**, a dot denotes the number of protrusions per donor cell in a transplant at a given time point. Data shown as mean ± s.e.m. (**b**, **c**, **f** and **g**) or s.d. (**d**). Kruskal–Wallis test. ****P < 0.0001, **P = 0.0013 (shield wt versus 75% wt); **P = 0.0034 (shield wt versus 50% +DN-Rac1); ns, not significant. ***P = 0.0007 (50% wt versus shield +Nodal) (**b**, and **f**). Dorsal view (cross-section in **a** and **e**). Scale bars: 10 μm (**a** and **e**).
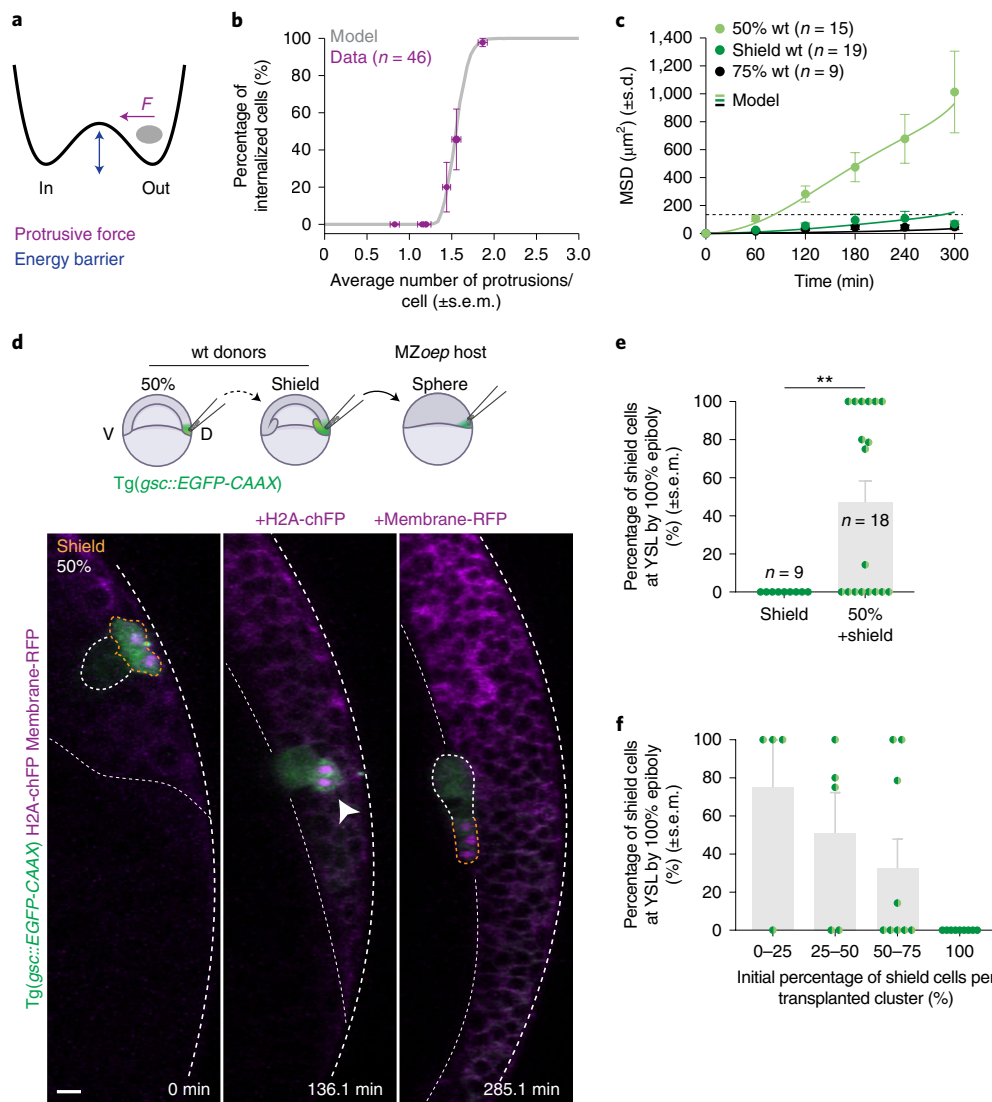
Fig. 3 | Early mesendoderm cells are above the motility-driven (un)jamming threshold and can act as leaders pulling late on follower cells. a, Schematic representation of a toy model for motility-driven (un)jamming. **b,** Percentage of internalized donor cells as a function of the average number of protrusions per cell across all experimental conditions (purple, also plotted in Fig. 2c,g) and predicted by the model (grey, Supplementary Note; see also Extended Data Fig. 4f). **c,** MSD of donor mesendoderm cells, collected from embryos at 50% ($N = 9$), shield ($N = 12$) or 75% epiboly ($N = 8$) stage, or predicted by the model based on their experimentally measured average protrusiveness (see also Fig. 2b). The dashed line corresponds to the average cell size at 300 min (see Supplementary Note and Fig. 1i for the percentage of internalized donor cells for these transplants). **d,** High-resolution confocal images of co-transplanted mesendoderm donor cells, collected from 50% epiboly and shield stage embryos (schematic representation on top). All donor cells express *gsc::EGFP-CAAX* (green) and can be distinguished by H2A-chFP expression (magenta,

nuclei). MZ*oep* host embryo expresses low levels of *gsc::EGFP-CAAX* (green) and Membrane-RFP (magenta). Dashed white lines indicate EVL and YSL. Thick dashed white and yellow lines outline donor cells collected from 50% epiboly and shield stage embryos, respectively. White arrowhead points at co-transplanted donor cells forming a cohesive heterotypic cluster. Start of acquisition after transplantation at 0 min. **e,** Percentage of internalized mesendoderm donor cells, collected from shield stage embryos, when transplanted alone or together with early donor cells (50% epiboly) ($N = 9$). **f,** Percentage of internalized mesendoderm donor cells, collected from shield stage embryos, as a function of the initial composition of co-transplanted clusters ($n = 18$, $N = 9$). Only cohesive heterotypic clusters were included in the analysis shown in **e** and **f** (see also Extended Data Fig. 6a). Data shown as mean ± s.e.m. (**b**, **e** and **f**) or s.d. (**c**). Mann–Whitney test (two-sided). *******P* = 0.0084 (**f**). Dorsal view (cross-section in **d**). Scale bar 20 μm (**d**).

value of cell protrusiveness is necessary for internalization (Fig. 2g and Extended Data Fig. 3g–k), we found that this moderate increase in cell protrusiveness was accompanied by a strong increase in the internalization competence of these progenitors. Moreover, blocking this mild increase in cell protrusiveness in Nodal-overexpressing shield stage mesendoderm donor cells, by co-expressing low amounts of DN-Rac1, drastically reduced their internalization capacity to levels similar to uninduced stage-matched wt cells (Fig. 2e–g and Extended Data Fig. 3g–m).

To quantitatively understand the non-linear relationship between mesendoderm cell protrusiveness and internalization competence, we examined a one-dimensional toy model of motility-driven (un)jamming[33], where mesendoderm cell clusters at a time *t* experience a bistable energy landscape $V(z)$ (that is, must overcome an energy barrier to drive cellular rearrangements along the z-axis within the host tissue) and can move inwards as a result of a balance of directed motility forces $F(t)$ and surrounding friction ζ (Fig. 3a):

$$-\zeta \dot{z}(t) + F(t) - \partial_z V(z) = 0.$$

In this simple model, mesendoderm cell clusters can locally unjam, and thus are internalization-competent, if their directed motility force overcomes a critical value (Extended Data Fig. 4a–a''). When taking into account the temporal stochasticity in cell protrusiveness measured in vivo (±20% of normalized variance in protrusion number per cell; Extended Data Fig. 4b–e) via an Ornstein–Uhlenbeck equation for cell motility forces, the model predicted a phase diagram with three regions: for low or high average protrusive/motility forces, simulated mesendoderm cells have close to 0% or 100% probability of undergoing internalization, respectively, whereas in a narrow region around the critical point, internalization outcomes are characterized by high variability and become intermediate (Extended Data Fig. 4a', f–h and Supplementary Note). This variability emerges since clusters with average migration forces below, yet close to, the threshold can still transiently exert larger forces, allowing some of them to internalize (Extended Data Figs. 2b–d and 4c–e). Importantly, these quantitative predictions closely matched both the average (Fig. 3b) and individual (Extended Data Fig. 4f) internalization outcomes as a function of mesendoderm donor cell protrusiveness across all experimental conditions. This model also quantitatively captured the MSD of internalization-competent and internalization-incompetent cells across all conditions (Fig. 3c and Extended Data Fig. 4i,j), further supporting that small changes in mesendoderm cell protrusiveness are sufficient to account for large changes in internalization outcomes.

Finally, we asked whether cell–cell adhesion and cortical contractility, previously implicated in controlling supracellular motility transitions in in vitro cell monolayers[33,40,41], might also affect the competence for mesendoderm cell internalization. Measuring donor cell cluster compaction, as readout for the balance of cell–cell adhesion and contractility[42], revealed a trend of increasing sphericities with decreasing internalization competence of mesendoderm cells in time, yet no such correlation could be found in the perturbation experiments (Extended Data Fig. 5a,b). To nonetheless functionally test the role of cell compaction in determining internalization outcomes, we injected previously characterized morpholinos (MO) targeted against E-cadherin (E-Cad)[43] to reduce cell–cell adhesion in late mesendoderm progenitors (Extended Data Fig. 5c,d). While their compaction was reduced to values similar to those of early cells (Extended Data Fig. 5a,b,e,f), late *e-cad-MO*-injected donor cell clusters still failed to undergo internalization upon transplantation (Extended Data Fig. 5g–i'). Collectively, this suggests that Nodal signalling-dependent control of protrusiveness, rather than cell–cell adhesion and contractility (Extended Data Fig. 5j,j'), constitutes the central mechanism controlling the cell-autonomous capacity of mesendoderm progenitors to internalize.

Early mesendoderm progenitors can act as leaders to pull late followers inwards

Our data so far suggest that only mesendoderm progenitors above a threshold of Nodal signalling, and thus protrusive forces, can locally unjam and autonomously internalize. Given that Nodal forms a signalling gradient peaking at the margin[35–39] and decaying in time (Fig. 2d and Extended Data Fig. 2k), this suggests that only a small population of cells, spatially and temporally restricted to the margin at early gastrulation stages, can drive the unjamming/cell rearrangements required to initiate internalization movements. But how would then later cells internalize? One possibility is that mesendoderm cells undergo collective migration at the tissue scale, where highly protrusive early internalization-competent cells act as 'leaders' that mechanically pull internalization-incompetent 'followers' inwards.

To test this, we co-transplanted marginal mesendoderm cells from early (50% epiboly) and late (shield) donor embryos into MZ*oep* host embryos (Figs. 1h,i and 3d and Supplementary Video 2). Remarkably, we found that early and late cells migrated as a heterotypic cell cluster towards the inside of the blastoderm, with early cells preferentially positioned at the leading edge of the cluster and late cells following behind (Fig. 3d,e and Supplementary Video 4). As expected from a leader–follower organization, clusters mainly composed of early cells were more likely to internalize, while clusters mainly composed of late cells remained at the blastoderm surface (Fig. 3f). When such heterotypic clusters split at the boundary between early and late cells, early cells still internalized, while late cells remained at the blastoderm surface (Extended Data Fig. 6a,b), consistent with late cells being mechanically pulled by early cells to overcome local energy barriers and collectively migrate inwards.

Collective mesendoderm migration initiates ordered and pattern-preserving internalization movements in vivo

To determine the relevance of our observations from the transplantation assays for endogenous mesendoderm internalization, we first analysed cell protrusion formation in internalizing dorsal mesendoderm cells, mosaically labelled for F-actin, during in vivo gastrulation. Consistent with our previous observations, we found a higher average number and length of protrusions in marginal mesendoderm cells internalizing early compared with later stages of gastrulation (Extended Data Fig. 6c–j). Next, we asked whether the parameters derived from the transplants and in vivo Nodal signalling measurements could reproduce the large-scale internalization movements in vivo. For this, we employed a minimal numerical framework, previously used to study active (un)jamming in cell monolayers[44,45], and simulated cells as motile adhesive particles subject to the main morphogenetic forces acting at the blastoderm margin: epiboly, internalization and anterior-directed migration of internalized mesendoderm progenitors (Fig. 4a, Extended Data Fig. 7a–l and Supplementary Note).

Fig. 4 | A spatiotemporal pattern of leader-to-follower cells, encoded by Nodal signalling, initiates robust mesendoderm internalization. a, Schematic representation of the two-dimensional (2D) particle-based model. Particles are colour-coded for Nodal signalling activity. Dashed line indicates the YSL. **b**, Numerical simulations of wt mesendoderm internalization, based on the experimentally measured Nodal signalling gradient along the anteroposterior (AP) axis at gastrulation onset (Supplementary Note). Colour code and dashed line as in **a**. **c**, Correlation between mesendoderm cell position pre- and post-internalization in wt simulations ($R^2 = 0.64$) and wt embryos ($R^2 = 0.63$, $N = 6$; see also Fig. 1f and Supplementary Note). Dashed line indicates perfect conservation of the relative cell position during internalization ($R^2 = 1$). **d**, High-resolution confocal images of wt and MZ*lefty1/2* embryos stained for DAPI (grey, nuclei) and pSmad2/3 (magenta) at 50% epiboly stage. Dashed lines indicate deep cell margin. **e**, Normalized intensity of nuclear pSmad2/3 as a function of the distance to the blastoderm margin in wt and MZ*lefty1/2* embryos at 50% epiboly stage ($N = 3$). **f**, Numerical simulations of MZ*lefty1/2* mesendoderm internalization, based on the experimentally measured Nodal signalling gradient along the AP

axis at gastrulation onset (Supplementary Note). Colour code and dashed line as in **a**. **g**, High-resolution confocal images of axial mesendoderm internalization, marked by *gsc::EGFP-CAAX* expression (green), in a MZ*lefty1/2* embryo. H2A-chFP (magenta) marks all cell nuclei. Dashed white lines indicate the EVL and YSL. Arrowheads indicate the position of four cells during internalization (dark-green arrowheads highlight a dividing mesendoderm cell and its daughters). Internalization onset at 0 min. **h,i**, Individual tracks of the mesendoderm cells shown in **g** at internalization onset (**h**) and 60 min later (**i**). Colour code corresponds to the initial distance of internalizing cells to the blastoderm margin. **j**, Correlation between cell position pre- and post-internalization in MZ*lefty1/2* embryos ($N = 6$; see Supplementary Note). Dashed line as in **c**, and colour code as in **h** and **i**. **k**, Correlation between mesendoderm cell position pre- and post-internalization in MZ*lefty1/2* simulations ($R^2 = -1.5$) and MZ*lefty1/2* embryos ($R^2 = -1.6$, $N = 6$; see Supplementary Note). Dashed line as in **c**. Data shown as mean ± s.d. Dorsal view (top view in **d**, cross-section in **g**). Scale bars: 20 μm (**d** and **g**).

We first simulated a scenario where all mesendoderm cells have high internalization forces. In this case, internalization was not restricted to the margin, as all mesendoderm cells were able to locally drive rearrangement/unjamming and near-simultaneously internalized, resulting in a complete loss of positional order (Extended Data Fig. 7c). Conversely, lowering all internalization forces completely abolished mesendoderm internalization, as cells were unable to rearrange relative to one another (Extended Data Fig. 7d). Importantly,

when we inputted the experimentally measured Nodal gradient at the onset of gastrulation, assuming a linear relationship between Nodal signalling and internalization forces (Fig. 2a–g, Extended Data Figs. 2a–e,k, 3c–m and 6c–i and Supplementary Note), we found that only the marginal-most cells had sufficiently high forces to locally unjam. This restricted mesendoderm internalization to the margin (Fig. 4b and Supplementary Video 5) and resulted in a close quantitative agreement with the degree of positional order preservation
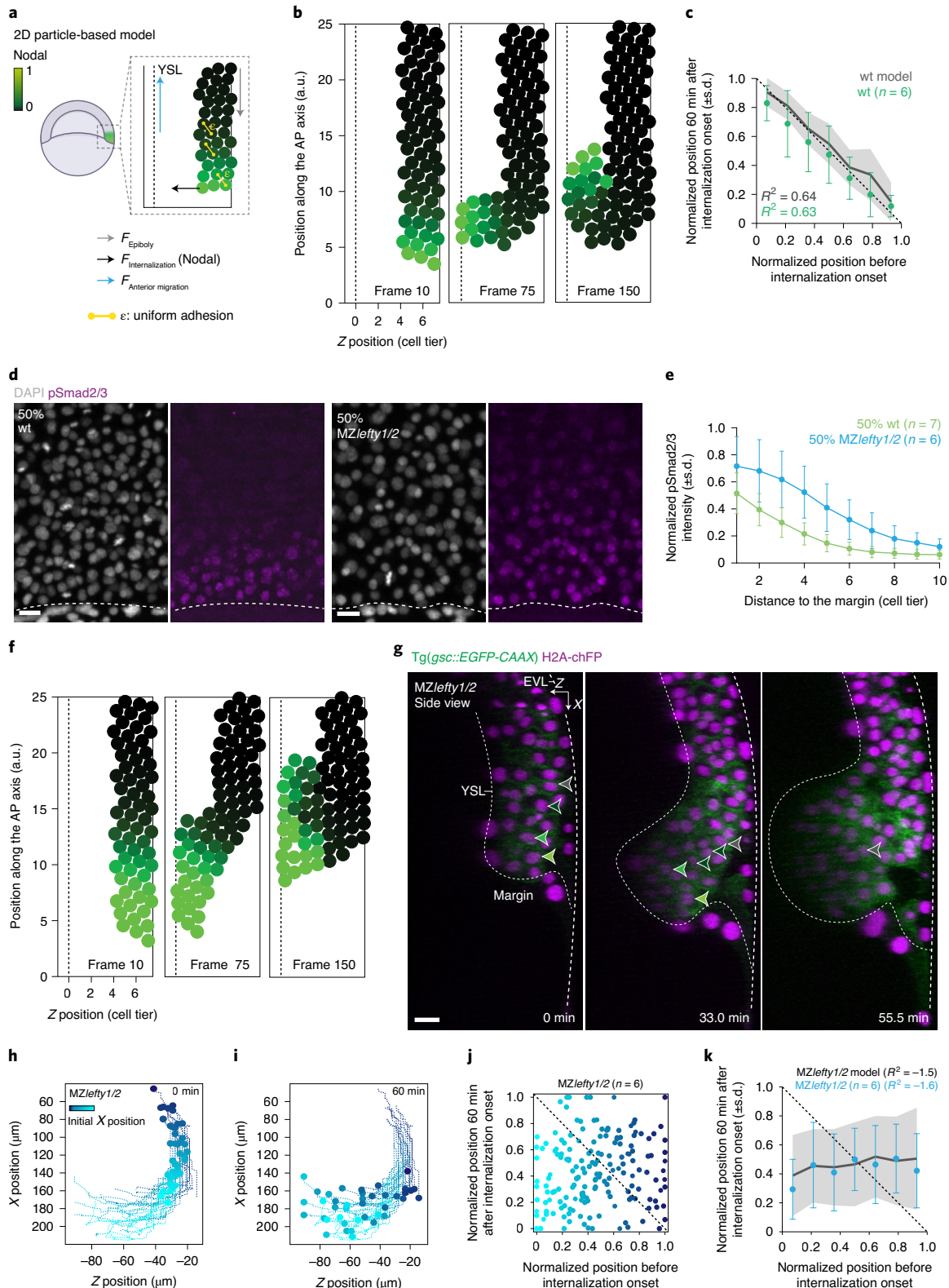
observed experimentally ($R^2 = 0.64$ versus $R^2 = 0.63$, respectively; Fig. 4c and Supplementary Note). This supports that, by subdividing the mesendoderm tissue into leader and follower cells, the Nodal signalling gradient initiates highly ordered, pattern-preserving internalization movements at the blastoderm margin.

Nodal signalling-encoded ratio of leader and follower cells is critical for ordered tissue internalization in vivo

To further challenge this model, we asked whether the shape of the Nodal signalling gradient is critical for ordered mesendoderm internalization. To this end, we turned to maternal-zygotic mutants of the Nodal inhibitors *lefty1/2* (MZ*lefty1/2*), which exhibit increased Nodal signalling and mesendoderm specification[46]. Consistent with previous findings[46], MZ*lefty1/2* embryos displayed higher peak levels of Nodal signalling and an expanded gradient (Fig. 4d,e and Extended Data Fig. 8a,b). We thus reasoned that this expanded Nodal gradient should increase the number of leader cells above the critical motility force for local (un)jamming. When using the experimentally measured Nodal signalling gradient in MZ*lefty1/2* embryos as an input parameter for our particle-based model (leaving all other parameters unchanged; Supplementary Note), the simulations predicted a highly disorganized internalization process, where positional order was lost (Fig. 4f and Supplementary Video 5). As expected, this was due to an increased number of leader cells simultaneously internalizing at multiple locations ($R^2 = -1.5$; Fig. 4f,k, Supplementary Video 5 and Supplementary Note). Strikingly, tracking individual mesendoderm cells in MZ*lefty1/2* embryos at the onset of internalization revealed a similarly disordered process, closely matching our model predictions ($R^2 = -1.6$ versus $R^2 = -1.5$, respectively; Fig. 4g–k, Extended Data Fig. 8c,d and Supplementary Videos 5 and 6) and clearly contrasting our previous observations of wt embryos and corresponding simulations (Figs. 1b–f and 4c, Extended Data Fig. 1b and Supplementary Videos 1 and 5).

Finally, in line with the assumption that an expanded Nodal signalling gradient increases the number of leader cells by increasing cell protrusiveness, we found that MZ*lefty1/2* mesendoderm cells displayed not only a prolonged competence to unjam and autonomously internalize upon transplantation (Extended Data Fig. 8a,b,e–h) but also a sustained increase in the average number and length of protrusions compared with wt cells (Extended Data Figs. 6c–h and 8j–m). In contrast to this, transplanted wt and MZ*lefty1/2* mesendoderm cells formed clusters of similar compaction (Extended Data Fig. 8i), arguing against Nodal signalling regulating their differential internalization competence by changing the balance between cell–cell adhesion and contractility. Collectively, these findings argue that the shape of the Nodal signalling gradient is critical to set a low ratio of leader to follower cells, essential for triggering collective and orderly mesendoderm internalization.

Nodal signalling-mediated preferential adhesion is required for preserving positional information during later stages of mesendoderm internalization

For collective and ordered mesendoderm internalization to occur at the tissue scale, leader cells need to establish and maintain strong cell–cell contacts with their immediate followers to transmit pulling forces. While at the start of mesendoderm internalization, cells are mainly in contact with their immediate neighbours, once internalization movements are underway, internalized mesendoderm cells will also come into contact with not-yet-internalized progenitors over the newly formed tissue boundary. To probe whether such cross-boundary contacts affect positional order during later stages of gastrulation, we extended our tracking analysis of mesendoderm internalization and anterior migration both in the simulations and in vivo. Interestingly, we found that positional order was increasingly lost in the simulations (Fig. 5a, Supplementary Video 5 and Supplementary Note), but still maintained in vivo ($R^2 = 0.36$ versus $R^2 = 0.83$, respectively; Fig. 5b).

To understand this discrepancy, we computed average velocity maps for internalized mesendoderm cells during anterior migration. In the simulations, the internalized mesendoderm cells migrating away from the blastoderm margin displayed uniformly lower velocities near the forming tissue boundary than close to the YSL, while in vivo this effect was only detectable at the marginal-most region of the blastoderm (Extended Data Fig. 9a–c). The strong velocity gradient emerging at the forming tissue boundary in the simulations was due to strong adhesion between internalized and not-yet-internalized cells, resulting in extensive cell–cell rearrangements mainly along the tissue boundary and, consequently, loss of positional order within the internalized tissue ($R^2 = 0.36$; Extended Data Fig. 9b, Fig. 5a,b and Supplementary Video 5). Since such velocity gradients were restricted to the marginal-most region of the blastoderm in vivo, positional order was well preserved even at later stages of gastrulation ($R^2 = 0.83$; Extended Data Fig. 9c and Fig. 5b).

This divergence between model predictions and experiments suggests that, in contrast to our original assumption of uniform cell–cell adhesion, adhesion might instead be regulated in a position-dependent manner, thereby minimizing cross-boundary effects. Given previous findings that Nodal signalling modulates cell–cell adhesion[20,24,47–49], we computationally addressed two scenarios: differential adhesion, where the Nodal signalling gradient is translated into a gradient of absolute adhesion strength, and heterotypic/preferential adhesion, where Nodal signalling determines preferential adhesion among mesendoderm cells, with stronger cell–cell adhesion between cells located at similar positions within the Nodal gradient and, thus, with similar Nodal signalling activity (Extended Data Fig. 9d,e and Fig. 5c). Simulations incorporating heterotypic/preferential adhesion, but

Fig. 5 | Leader–follower cohesion contributes to orderly mesendoderm internalization and migration. a, Numerical simulation of wt mesendoderm internalization, corresponding to a time point later than in Fig. 4b. Particles are colour-coded for Nodal signalling activity. Dashed line indicates the YSL. Arrowheads denote mis-localized internalized cells. AP: anterior-posterior axis. **b**, Correlation between cell position at later stages of tissue internalization in wt simulations assuming uniform adhesion ($R^2 = 0.36$) and in wt embryos ($R^2 = 0.83$, $N = 6$; Supplementary Note). Dashed line indicates perfect conservation of the relative cell position during internalization ($R^2 = 1$). **c**, Schematic representation of the 2D particle-based model assuming Nodal-dependent heterotypic adhesion. Colour code and dashed line as in **a**. **d**, Numerical simulations of wt mesendoderm internalization assuming Nodal signalling-dependent heterotypic adhesion (other parameters as in Fig. 4b; Supplementary Note). Colour code and dashed line as in **a**. **e**, Correlation between cell position at later stages of tissue internalization in wt simulations assuming Nodal signalling-dependent heterotypic adhesion ($R^2 = 0.75$) and in wt embryos ($R^2 = 0.83$, $N = 6$; Supplementary Note). Dashed line as in **b**. **f**, High-resolution confocal images of co-transplanted mesendoderm donor cells, collected from 50% and 75% epiboly

or 50%, shield and 75% epiboly stage embryos (schematics on top). All donor cells express *gsc::EGFP-CAAX* (green) and can be distinguished by H2A-chFP expression (magenta, nuclei; 75%) or H2A-chFP and Membrane-RFP co-expression (magenta; shield). MZ*oep* hosts express low levels of *gsc::EGFP-CAAX* (green) and Membrane-RFP (magenta). Dashed white lines indicate the EVL and YSL. Thick dashed lines outline donor cells collected from 50% (white), shield (yellow) and 75% epiboly (orange) embryos. Arrowheads point at cohesive heterotypic clusters. **g**, Percentage of co-transplanted late mesendoderm donor cells (shield, $N = 10$; 75%, $N = 9$; shield+75%, $N = 6$) that remain clustered with early cells (50% epiboly) until the end of epiboly. Dots correspond to the individual experiments and the graph shows the average. The points and error bars are mean ± s.e.m. **h**, Number of homotypic or heterotypic cell–cell contacts lost upon the final splitting of mesendoderm cell clusters of different compositions (see **g** for *n* and *N*), normalized to the number of transplanted clusters. **i**, Working model for the dual mechanical role of Nodal signalling in zebrafish gastrulation. Data shown as mean ± s.d. (**b** and **e**) or s.e.m. (**g**). Kruskal–Wallis test. ****$P < 0.0001$; ns, not significant (**g**). Dorsal view (cross-section in **f**). Scale bars: 20 μm (**f**).

not differential adhesion, robustly reproduced the experimentally observed orderly cell movements even at later stages of gastrulation ($R^2 = 0.75$ and $R^2 = 0.16$ for heterotypic or differential adhesion, respectively, versus $R^2 = 0.83$ in vivo; Fig. 5d,e, Extended Data Fig. 9e–j and Supplementary Video 5), as well as the nearly uniform velocities for internalized mesendoderm cells migrating at a distance from the margin (Extended Data Fig. 9c, k; see also Extended Data Fig. 10a–g for 3D simulations and Supplementary Note).

To experimentally test this model assumption, we performed a set of co-transplantation experiments, where donor cells with different Nodal signalling activity were co-transplanted and monitored for their ability to preserve cluster cohesiveness, a functional readout of cell–cell adhesion strength in this context (Fig. 5f). We reasoned that, for Nodal-mediated heterotypic adhesion, the integrity of a leader–follower cluster should be preserved where differences in Nodal signalling are small but lost once these differences increase (Extended Data Fig. 9d).
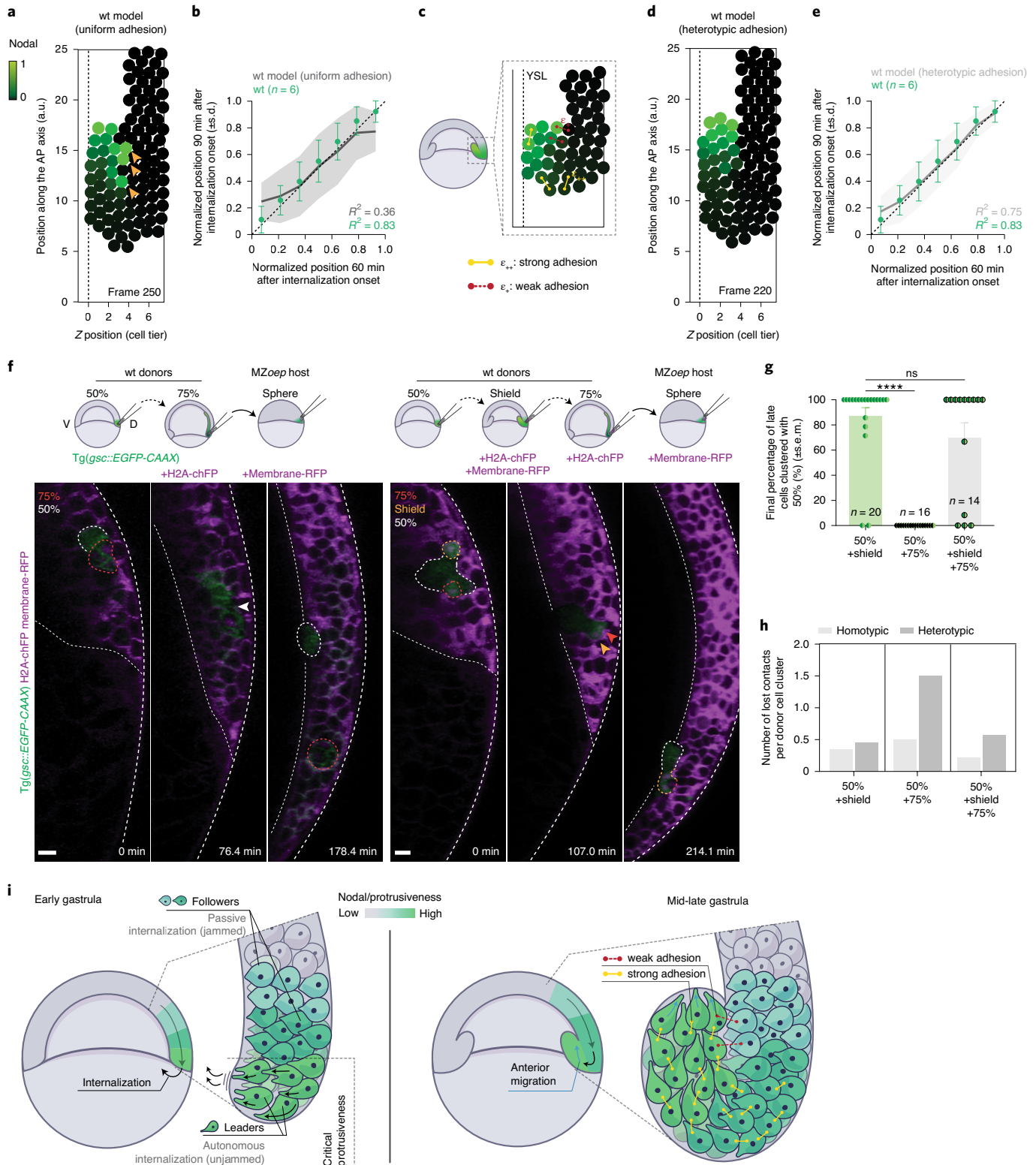
Our previous co-transplantation experiments with mesendoderm progenitors from donor embryos at 50% epiboly and shield stage showed that cluster integrity was well preserved over time (Fig. 3d–f, Extended Data Fig. 6a,b and Supplementary Video 4). In contrast, when we co-transplanted mesendoderm cells from donor embryos at 50% and 75% epiboly stage (comparably larger differences in Nodal activity; Fig. 2d and Extended Data Fig. 2k), cluster integrity was lost, mainly due to heterotypic contact breakage, with early (50% epiboly) cells typically internalizing and late (75% epiboly) cells remaining jammed in superficial layers of the blastoderm (Fig. 5f–h and Supplementary Video 7).

To further challenge our model of Nodal-mediated heterotypic adhesion, we again co-transplanted mesendoderm cells from 50% and 75% epiboly stage donor embryos, but this time using Nodal-overexpressing 75% epiboly stage donor embryos. With this, we kept the differences in developmental time between co-transplanted cells constant, but narrowed their overall difference in Nodal signalling activity. Accordingly, Nodal-overexpressing cells exhibit an anterior axial mesendoderm fate at 75% epiboly (Extended Data Fig. 3a,b), as expected from cells exposed to high Nodal signalling[8,11,50–52]. In these co-transplantations, cluster cohesion was strongly enhanced (Extended Data Fig. 9l–n), supporting that adhesion strength at heterotypic contacts is modulated by the differences in Nodal signalling activity.

As an ultimate test of our model, we then co-transplanted mesendoderm cells from 50% epiboly, shield and 75% epiboly stage donor embryos (Fig. 5f, right). In such triple clusters, shield cells would be expected to mediate adhesion between early and late cells (Extended Data Fig. 9d). Strikingly, the proportion of cohesive transplants was strongly increased when compared with clusters composed solely of 50% and 75% mesendoderm cells (Fig. 5f–h). Moreover, we observed that, in some cases, cohesive triple clusters completed their internalization, with early cells positioned at the leading edge, followed by shield and then 75% epiboly cells (Fig. 5f, right), mimicking the adhesion sequence of the gastrulating embryo.

Our study reveals that a morphogen gradient encodes a sharp mechanical switch in cell migration competence in vivo, resembling a motility-driven (un)jamming transition, previously explored in cell monolayers via self-propelled vertex models[33,41,53]. Such a motility-driven (un)jamming transition constitutes a complementary mechanism to recent in vitro[40,54] and in vivo[55–61] studies, where cell movement/uncaging is used as a proxy for tissue (un)jamming and is mechanistically controlled by changes in the cells' adhesive and contractile properties[54,56–58,61]. In our study, in contrast, graded cell motility (downstream of Nodal signalling) functions as the control parameter triggering this transition, thereby determining the ability of a subset of mesendoderm cells to locally unjam and migrate towards the YSL (Fig. 5i). This morphogen-encoded (un)jamming transition provides insight into not only the effector mechanisms by which mechanochemical signalling converts a graded upstream signal into the discrete mechanical domains necessary for collective morphogenesis, but also the functional relevance of (un)jamming transitions in development[28–30]. Indeed, it ensures that mesendoderm internalization remains restricted to the blastoderm margin, a prerequisite for collective and ordered tissue internalization.

Collective migration, a fundamental process in a number of developmental, homeostatic and pathological settings, promotes directed migration by strengthening the response of cells to extrinsic guidance cues and/or driving supracellular polarization[62–64]. This study points at another important function of collective migration in preserving tissue patterning during complex 3D movements. A critical determinant of this collective mode of tissue internalization is the ability of leader cells to effectively pull on their immediate followers. Interestingly, our findings support that mesendoderm cells originally at a similar position within the Nodal signalling gradient before internalization not only acquire a similar fate[50,51,65–67], but also display preferential adhesion.

Such a preferential adhesion mechanism, previously proposed to be efficient at driving cell sorting[68], is therefore also critical for collective migration. Indeed, it both provides strong cohesion along the path of internalization, by efficiently transmitting pulling forces from leaders to their designated follower cells, and minimizes interactions across the forming tissue boundary during later stages of internalization and anterior migration (Fig. 5i, right). This also suggests a dual mechanical role of Nodal signalling in mesendoderm collective migration, by controlling both cell protrusion forces to regulate leader–follower proportions and cell–cell adhesion forces to ensure cohesion between the leader and follower domains.

How the biochemical signals determining embryo patterning and the mechanical forces driving morphogenesis are integrated is still a matter of intense research. The temporal sequence in which these two processes occur in development is important, particularly when tissue morphogenesis follows patterning, since mechanically driven tissue flows are likely to perturb the initial pattern by dynamically changing the spatial arrangement of cells within the tissue[69]. This is relevant for zebrafish gastrulation, where Nodal signalling-mediated patterning occurs primarily in blastula and early gastrula stages[12], before or concomitant with the extensive 3D migratory movements associated with germ layer internalization. Our findings identify a cross-scale mechanism where a morphogen gradient ensures pattern preservation despite large-scale morphogenesis, by functioning as both a morphogen controlling cell fate specification and a 'mechanogen'[70] triggering collective migration through a motility-driven (un)jamming transition. Since morphogen gradients are highly conserved in vertebrate development[1,13,14,71,72], similar mechanochemical gradients might be relevant in other developmental and disease-related processes, thereby constituting a general principle coordinating tissue patterning and morphogenesis.

Online content

Any methods, additional references, Nature Research reporting summaries, source data, extended data, supplementary information, acknowledgements, peer review information; details of author contributions and competing interests; and statements of data and code availability are available at https://doi.org/10.1038/s41567-022-01787-6.

References

1. Rogers, K. W. & Schier, A. F. Morphogen gradients: from generation to interpretation. *Annu. Rev. Cell Dev. Biol.* **27**, 377–407 (2011).
2. Solnica-Krezel, L. & Sepich, D. S. Gastrulation: making and shaping germ layers. *Annu. Rev. Cell Dev. Biol.* **28**, 687–717 (2012).
3. Gilmour, D., Rembold, M. & Leptin, M. From morphogen to morphogenesis and back. *Nature* **541**, 311–320 (2017).
4. Bailles, A., Collinet, C., Philippe, J.-M., Lenne, P.-F. & Munro, E. Genetic induction and mechanochemical propagation of a morphogenetic wave. *Nature* **572**, 467–473 (2019).
5. Collinet, C. & Lecuit, T. Programmed and self-organized flow of information during morphogenesis. *Nat. Rev. Mol. Cell Biol.* **22**, 245–265 (2021).
6. Guignard, L. et al. Contact area-dependent cell communication and the morphological invariance of ascidian embryogenesis. *Science* **369**, eaar5663 (2020).
7. Tsai, T. Y. C. et al. An adhesion code ensures robust pattern formation during tissue morphogenesis. *Sci. (80-.).* **370**, 113–116 (2020).
8. Zinski, J., Tajer, B. & Mullins, M. C. TGF-β family signaling in early vertebrate development. *Cold Spring Harb. Perspect. Biol.* **10**, a033274 (2018).
9. Rogers, K. W. & Müller, P. Nodal and BMP dispersal during early zebrafish development. *Dev. Biol.* **447**, 14–23 (2019).

10. Pinheiro, D. & Heisenberg, C. P. in *Current Topics in Developmental Biology* (ed. Solnica-Krezel, L.) vol 136, pp 343–375 (Academic, 2020).

11. Economou, A. D. & Hill, C. S. in *Current Topics in Developmental Biology* (ed. Briscoe, J.) vol. 137, pp 363–389 (Academic, 2020).

12. Hagos, E. G. & Dougan, S. T. Time-dependent patterning of the mesoderm and endoderm by Nodal signals in zebrafish. *BMC Dev. Biol.* **7**, 22 (2007).

13. Rivera-Pérez, J. A. & Hadjantonakis, A. K. The dynamics of morphogenesis in the early mouse embryo. *Cold Spring Harb. Perspect. Biol.* **7**, a015867 (2015).

14. Bardot, E. S. & Hadjantonakis, A. K. Mouse gastrulation: coordination of tissue patterning, specification and diversification of cell fate. *Mech. Dev.* **163**, 103617 (2020).

15. Carmany-Rampey, A. & Schier, A. F. Single-cell internalization during zebrafish gastrulation. *Curr. Biol.* **11**, 1261–1265 (2001).

16. David, N. B. & Rosa, F. M. Cell autonomous commitment to an endodermal fate and behaviour by activation of Nodal signalling. *Development* **128**, 3937–3947 (2001).

17. Montero, J.-A. et al. Shield formation at the onset of zebrafish gastrulation. *Development* **123**, 1187–1198 (2005).

18. Townes, P. L. & Holtfreter, J. Directed movements and selective adhesion of embryonic amphibian cells. *J. Exp. Zool.* **128**, 53–120 (1955).

19. Wacker, S., Grimm, K., Joos, T. & Winklbauer, R. Development and control of tissue separation at gastrulation in. *Xenopus. Dev. Biol.* **224**, 428–439 (2000).

20. Krieg, M. et al. Tensile forces govern germ-layer organization in zebrafish. *Nat. Cell Biol.* **10**, 429–436 (2008).

21. Maître, J.-L. et al. Adhesion functions in cell sorting by mechanically coupling the cortices of adhering cells. *Sci. (80-.).* **338**, 253–256 (2012).

22. Ninomiya, H. et al. Cadherin-dependent differential cell adhesion in *Xenopus* causes cell sorting in vitro but not in the embryo. *J. Cell Sci.* **125**, 1877–1883 (2012).

23. Krens, S. F. G. et al. Interstitial fluid osmolarity modulates the action of differential tissue surface tension in progenitor cell segregation during gastrulation. *Development* **144**, 1798–1806 (2017).

24. Giger, F. A. & David, N. B. Endodermal germ-layer formation through active actin-driven migration triggered by N-cadherin. *Proc. Natl Acad. Sci. U. S. A.* **114**, 10143–10148 (2017).

25. Liu, Z., Woo, S. & Weiner, O. D. Nodal signaling has dual roles in fate specification and directed migration during germ layer segregation in zebrafish. *Development* **145**, dev163535 (2018).

26. Keller, P. J., Schmidt, A. D., Wittbrodt, J. & Stelzer, E. H. K. Reconstruction of zebrafish early embryonic development by scanned light sheet microscopy. *Sci. (80-.).* **322**, 1065–1069 (2008).

27. Shah, G. et al. Multi-scale imaging and analysis identify pan-embryo cell dynamics of germlayer formation in zebrafish. *Nat. Commun.* **10**, 5753 (2019).

28. Atia, L., Fredberg, J. J., Gov, N. S. & Pegoraro, A. F. Are cell jamming and unjamming essential in tissue development. *Cells Dev.* https://doi.org/10.1016/j.cdev.2021.203727 (2021).

29. Lawson-Keister, E. & Manning, M. L. Jamming and arrest of cell motion in biological tissues. *Curr. Opin. Cell Biol.* **72**, 146–155 (2021).

30. Hannezo, E. & Heisenberg, C. P. Rigidity transitions in development and disease. *Trends Cell Biol.* https://doi.org/10.1016/j.tcb.2021.12.006 (2022).

31. Iimura, T. & Pourquié, O. Collinear activation of Hoxb genes during gastrulation is linked to mesoderm cell ingression. *Nature* **442**, 568–571 (2006).

32. Gritsman, K. et al. The EGF-CFC protein one-eyed pinhead is essential for nodal signaling. *Cell* **97**, 121–132 (1999).

33. Bi, D., Yang, X., Marchetti, M. C. & Manning, M. L. Motility-driven glass and jamming transitions in biological tissues. *Phys. Rev. X* **6**, 021011 (2016).

34. Woo, S., Housley, M. P., Weiner, O. D. & Stainier, D. Y. R. Nodal signaling regulates endodermal cell motility and actin dynamics via Rac1 and Prex1. *J. Cell Biol.* **198**, 941–952 (2012).

35. Harvey, S. A. & Smith, J. C. Visualisation and quantification of morphogen gradient formation in the zebrafish. *PLoS Biol.* **7**, e1000101 (2009).

36. Dubrulle, J. et al. Response to nodal morphogen gradient is determined by the kinetics of target gene induction. *eLife* **4**, 1–27 (2015).

37. Boxtel, A. L. Van et al. A temporal window for signal activation dictates the dimensions of a nodal signaling domain. *Dev. Cell* **35**, 175–185 (2015).

38. Boxtel, A. L. Van, Economou, A. D., Heliot, C. & Hill, C. S. Long-range signaling activation and local inhibition separate the mesoderm and endoderm lineages. *Dev. Cell* **44**, 1–13 (2017).

39. Schauer, A., Pinheiro, D., Hauschild, R. & Heisenberg, C. P. Zebrafish embryonic explants undergo genetically encoded self-assembly. *eLife* **9**, e55190 (2020).

40. Park, J. A. et al. Unjamming and cell shape in the asthmatic airway epithelium. *Nat. Mater.* **14**, 1040–1048 (2015).

41. Mitchel, J. A. et al. In primary airway epithelial cells, the unjamming transition is distinct from the epithelial-to-mesenchymal transition. *Nat. Commun.* **11**, 1–14 (2020).

42. Turlier, H. & Maître, J. Mechanics of tissue compaction. *Semin. Cell Dev. Biol.* **48**, 110–117 (2015).

43. Babb, S. G. & Marrs, J. A. E-Cadherin regulates cell movements and tissue formation in early zebrafish embryos. *Dev. Dyn.* **230**, 263–277 (2004).

44. Garcia, S. et al. Physics of active jamming during collective cellular motion in a monolayer. *Proc. Natl Acad. Sci. U. S. A.* **112**, 15314–15319 (2015).

45. Sarkar, D., Gompper, G. & Elgeti, J. A minimal model for structure, dynamics, and tension of monolayered cell colonies. *Commun. Phys.* **4**, 36 (2021).

46. Rogers, K. W. et al. Nodal patterning without lefty inhibitory feedback is functional but fragile. *eLife* **6**, 1–20 (2017).

47. Ogata, S. et al. TGF-β signaling-mediated morphogenesis: modulation of cell adhesion via cadherin endocytosis. *Genes Dev.* **21**, 1817–1831 (2007).

48. Barone, V., Lang, M., Krens, S. F. G., Calin, C. G. & Heisenberg, C.-P. An effective feedback loop between cell–cell contact duration and morphogen signaling determines cell fate. *Dev. Cell* **43**, 1–14 (2017).

49. Ko, J. M. & Lobo, D. Continuous dynamic modeling of regulated cell adhesion: sorting, intercalation, and involution. *Biophys. J.* **117**, 1–14 (2019).

50. Gritsman, K., Talbot, W. S. & Schier, A. F. Nodal signaling patterns the organizer. *Development* **127**, 921–932 (2000).

51. Dougan, S. T., Warga, R. M., Kane, D. A., Schier, A. F. & Talbot, W. S. The role of the zebrafish nodal-related genes squint and cyclops in patterning of mesendoderm. *Development* **130**, 1837–1851 (2003).

52. Schier, A. F. & Talbot, W. S. Molecular genetics of axis formation in zebrafish. *Annu. Rev. Genet.* **39**, 561–613 (2005).

53. Malinverno, C. et al. Endocytic reawakening of motility in jammed epithelia. *Nat. Mater.* **16**, 587–596 (2017).

54. Devany, J., Sussman, D. M., Yamamoto, T., Manning, M. L. & Gardel, M. L. Cell cycle-dependent active stress drives epithelia remodeling. *Proc. Natl Acad. Sci. U. S. A.* **118**, e1917853118 (2021).

55. Atia, L. et al. Geometric constraints during epithelial jamming. *Nat. Phys.* **14**, 613–620 (2018).
56. Mongera, A. et al. A fluid-to-solid jamming transition underlies vertebrate body axis elongation. *Nature* **561**, 401–405 (2018).
57. Miroshnikova, Y. A. et al. Adhesion forces and cortical tension couple cell proliferation and differentiation to drive epidermal stratification. *Nat. Cell Biol.* **20**, 69–80 (2018).
58. Tetley, R. J. et al. Tissue fluidity promotes epithelial wound healing. *Nat. Phys.* **15**, 1195–1203 (2019).
59. Wang, X. et al. Anisotropy links cell shapes to tissue flow during convergent extension. *Proc. Natl Acad. Sci. U. S. A.* **117**, 13541–13551 (2020).
60. Jain, A. et al. Regionalized tissue fluidization is required for epithelial gap closure during insect gastrulation. *Nat. Commun.* **11**, 5604 (2020).
61. Petridou, N. I., Corominas-Murtra, B., Heisenberg, C.-P. & Hannezo, E. Rigidity percolation uncovers a structural basis for embryonic tissue phase transitions. *Cell* **184**, 1–15 (2021).
62. Mayor, R. & Etienne-Manneville, S. The front and rear of collective cell migration. *Nat. Rev. Mol. Cell Biol.* **17**, 97–109 (2016).
63. Norden, C. & Lecaudey, V. Collective cell migration: general themes and new paradigms. *Curr. Opin. Genet. Dev.* **57**, 54–60 (2019).
64. Jain, S. et al. The role of single-cell mechanical behaviour and polarity in driving collective cell migration. *Nat. Phys.* **16**, 802–809 (2020).
65. Rebagliati, M. R., Toyama, R., Fricke, C., Haffter, P. & Dawid, I. B. Zebrafish nodal-related genes are implicated in axial patterning and establishing left-right asymmetry. *Dev. Biol.* **199**, 261–272 (1998).
66. Xu, P.-F., Houssin, N., Ferri-Lagneau, K. F., Thise, B. & Thisse, C. Construction of a vertebrate embryo from two opposing morphogen gradients. *Sci. (80-.).* **344**, 87–89 (2014).
67. Schier, A. F. Nodal morphogens. *Cold Spring Harb. Perspect. Biol.* **1**, a003459 (2009).
68. Canty, L., Zarour, E., Kashkooli, L., François, P. & Fagotto, F. Sorting at embryonic boundaries requires high heterotypic interfacial tension. *Nat. Commun.* **8**, 157 (2017).
69. Fulton, T., Verd, B. & Steventon, B. The unappreciated generative role of cell movements in pattern formation. *R. Soc. Open Sci.* **9**, 211293 (2022).
70. Dasbiswas, K., Hannezo, E. & Gov, N. S. Theory of epithelial cell shape transitions induced by mechanoactive chemical gradients. *Biophys. J.* **114**, 968–977 (2018).
71. Pauklin, S. & Vallier, L. Activin/Nodal signalling in stem cells. *Development* **142**, 607–619 (2015).
72. Bénazéraf, B. et al. A random cell motility gradient downstream of FGF controls elongation of an amniote embryo. *Nature* **466**, 248–252 (2010).

Methods

Fish lines and husbandry

Zebrafish (*Danio rerio*) maintenance and handling was performed as described in ref. [73]. The following strains were used in this study: wt AB or ABxTL, Tg(*gsc::EGFP-CAAX*)[74], Tg(*mezzo:EGFP*)[75], MZ*oep*[32], MZ*lefty1/2*[46], MZ*oep*; Tg(*gsc::EGFP-CAAX*) and MZ*lefty1/2*; Tg(*gsc::EGFP-CAAX*). Mutant transgenic lines were generated by crossing the Tg(*gsc::EGFP-CAAX*) transgenic line with MZ*oep* or MZ*lefty1/2* mutants. Embryos were raised at 25–31 °C in E3 or Danieu's (58 mM NaCl, 0.7 mM KCl, 0.4 mM MgSO₄, 0.6 mM Ca(NO₃)₂, 5 mM HEPES, pH 7.6) media and staged as described previously[76].

Molecular biology

To synthesize messenger RNA (mRNA) for the dominant-negative version of Rac1a (DN-Rac1), Gateway technology (Invitrogen)[77] was used to create a pCS2 vector containing the mutated version of Rac1a. The coding sequence of *rac1a* (NCBI reference sequence NM_199771.1) was amplified using specific primers with additional Gateway recombination arms (5′-GGGGACAAGTTTGTACAAAAAAGCAGG CTTAATGCAGGCCATAAAGTGTG-3′ and 5′-GGGGACCACTTTG TACAAGAAAGCTGG GTATCACAGAAGGAGACATCTTCTC-3′) from a complementary DNA library of wt Tübingen embryos. The PCR product was recombined with *pDONR221* (Lawson#208) and the resulting entry clone was used as a template to create the DN-Rac1a construct. The Rac1a entry clone was amplified with specific primers (5′-GCTGTGGGAAAAAATTGCCTTCTGATCAG-3′ and 5′-CTGATCAGAAGGCAATT TTTTCCCACAGC-3′) and mutated at residue 17 to substitute a threonine by an asparagine (T17N) as described previously[78,79], using site-directed mutagenesis. The introduction of the mutation was verified by sequencing, and the DN-Rac1a entry clone was recombined with *pCSDest2* (Lawson #444) and *p3E-polyA* (Chien#302) to create the vector used for mRNA synthesis.

Embryo microinjections

mRNA synthesis (mMessage mMachine Kit, Ambion) and injections in 1- or 128-cell stage embryos were performed as described in ref. [73]. The following mRNAs were injected at 1-cell stage: 50–100 pg *H2A-chFP*[80], 30–50 pg *H2B-EGFP*[26], 50–100 pg *Membrane-RFP*[81], 75 pg *LifeAct-RFP*[82] and 7.5 pg *DN-Rac1* (this study). To constitutively activate Nodal signalling, 1-cell stage donor embryos were injected with 100 pg *Ndr2*[83] or *Ndr2-chFP*[84] mRNA and 2 ng of *sox32* morpholino (5′-GCATCCGGTCGAGATACATGCTGTT-3′, GeneTools), as described previously[20]. To reduce cell–cell adhesion in donor embryos, 1-cell stage embryos were injected with 4 ng of *e-cadherin* morpholino (*e-cad*, 5′-TAAATCGCAGCTCTTCCTTCCAACG-3′, GeneTools) or the *scramble* control morpholino (5′-ATGCCAGAGTTCTTACAGAAGCGAT-3′, Gene-Tools)[43,48,61]. To label F-actin in a mosaic fashion in wt or MZ*lefty1/2* embryos, a single blastomere was injected at 128-cell stage with 7.5 pg *LifeAct-RFP*[82].

Cell transplantation assays

Donor and host embryos were manually dechorionated with watchmaker forceps in Danieau's medium. Mesendoderm cells (2–30 cells) were collected from the dorsal margin, marked by EGFP-CAAX expression in Tg(*gsc::EGFP-CAAX*) embryos, or the ventral margin, marked by low EGFP expression in Tg(*mezzo::EGFP*) embryos, at different stages of gastrulation using a bevelled borosilicate needle (20 μm inner diameter with spike; Biomedical Instruments) connected to a syringe system mounted on a micromanipulator. Since embryos overexpressing Nodal and/or DN-Rac1 showed aberrant morphogenesis, sibling embryos injected only with a fluorescence reporter (H2A-chFP or LifeAct-RFP) were used as staging controls. In Nodal-overexpressing embryos, donor cells were collected from the margin. Donor cells were then transplanted into the dorsal or ventral margin, marked by expression of EGFP-CAAX or the region diametrically opposed to it, respectively,

in MZ*oep*; Tg(*gsc::EGFP-CAAX*) host embryos underneath the EVL (schematic representations in Fig. 1g and Extended Data Fig. 1g,j). The developmental stage of donor embryos is indicated in the figure, and unless stated otherwise, mesendoderm cells were transplanted into sphere stage MZ*oep* hosts.

In co-transplantation experiments, mesendoderm cells were sequentially collected from the dorsal margin of donor embryos at different developmental stages into the same bevelled borosilicate needle and then transplanted into the dorsal margin of sphere stage MZ*oep*; Tg(*gsc::EGFP-CAAX*) host embryos underneath the EVL (schematic representation in Figs. 3d and 5f). The order of collection of donor cells was purposely varied. In triple co-transplantation assays, mesendoderm cells were sequentially collected from 50%, shield and 75% epiboly embryos or 75%, shield and 50% epiboly stage embryos.

Whole-mount immunofluorescence

Wt, Nodal-overexpressing and MZ*lefty1/2* embryos were fixed at different stages of gastrulation in 4% paraformaldehyde (in PBS) overnight at 4 °C. After fixation, the samples were washed three or four times in PBS, dechorionated using watchmaker forceps and then transferred into methanol (100%) for storage at −20 °C for a minimum of 2 h. Whole-mount immunofluorescence for α-pSmad2/3 was performed as described previously[37] (with minor modifications as in ref. [39]). The samples were incubated overnight at 4 °C with the α-pSmad2/3 antibody (clone D27F4, cat. no. 8828, 1:1,000; Cell Signaling) and then the secondary antibody (Alexa Fluor 546 goat anti-rabbit IgG; Thermo Fisher Scientific, cat. no. A-11010, 1:500).

Control and *e-cadherin* MO-injected embryos were fixed at shield stage as detailed above. Whole-mount immunofluorescence for E-Cad was performed as described previously[85]. The samples were incubated overnight at 4 °C with the α-E-Cad antibody (rabbit anti-zebrafish E-Cad[21], 1:200) and then for 3–5 h at room temperature with the secondary antibody described above. To label the cell nuclei, DAPI (1:1,000) was added to the secondary antibody solution for 20 min at room temperature before the start of the last round of washes.

Whole-mount in situ hybridization

Wt and Nodal-overexpressing embryos were fixed at different stages of gastrulation in 4% paraformaldehyde (in PBS) overnight at 4 °C. After fixation, embryos were quickly washed three or four times in PBS, dechorionated using watchmaker forceps and, then, transferred into methanol (100%) for storage at −20 °C for a minimum of 2 h. In situ probes were synthesized from partial cDNA sequences using the MEGAscript T7 RNA polymerase kit (Thermo Fisher Scientific, cat. no. AM1334) with Roche digoxigenin (DIG)-modified nucleotides (Sigma-Aldrich, cat. no. 11277073910). Whole-mount in situ hybridization was performed as described previously[86] for *gsc* in situ hybridization (anti-DIG-AP Fab fragments, Roche, cat. no. 11093274910, 1:1,000). For *sox17* in situ hybridization, an extra proteinase K treatment (30 s; Invitrogen, cat. no. 25530049) was performed and 5% dextran sulphate (Sigma-Aldrich, cat. no. 31404) was added to the hybridization solution. The staining reaction was stopped simultaneously for all embryos. After staining, the samples were cleared with 100% ethanol and washed several times with PBS or PBS + 0.1% (w/v) Tween 20. The embryos were then mounted in a Petri dish containing small 2% agarose wells (800 μm × 800 μm; Microtissues) in PBS and imaged using an Olympus SZX 12 stereo microscope equipped with a QImaging Micropublisher 5.0 camera.

Image acquisition

For whole-embryo single-plane imaging, dechorionated embryos were mounted in a glass-bottom dish containing 2% agarose wells and immobilized in 0.6–0.7% low-melting-point agarose with the dorsal side of embryo oriented laterally. Imaging was performed using a Nikon Eclipse inverted wide-field microscope equipped with a Nikon 10×/NA 0.3 PH1 air objective and a fluorescent light source (Lumencor).

For live imaging experiments and fixed samples immunostained for pSmad2/3, dechorionated embryos were mounted and immobilized as described above with either the dorsal or the ventral side of embryo facing the objective. Imaging was performed using a LSM 880 or 800 upright microscope equipped with a Zeiss plan-apochromat 20×/NA 1.0 water-immersion objective. For high-magnification analysis of mesendoderm cell internalization and protrusion formation, as well as fixed samples immunostained for E-Cad, dechorionated embryos were mounted in a glass-bottom dish (35 mm; MatTek Corporation, cat. no. P35G-1.5-14-C) and immobilized in 0.6–0.7% low-melting-point agarose with the dorsal side of embryo facing the objective. The embryos were then imaged using a Zeiss LSM880 inverted microscope equipped with a Zeiss plan-apochromat 40×/NA 1.2 water-immersion objective.

Embryos were oriented using the Tg(*gsc::EGFP-CAAX*) line to identify both the dorsal and ventral sides of the embryo, as described for the cell transplantation assays. For live imaging experiments, mounted embryos were imaged in Danieau's media at 28.5 °C. Immunostained samples were imaged in PBS, and the imaging conditions were kept similar to enable comparison of fluorescence intensities across experimental conditions and replicates.

Data analysis

All image data analysis was performed using Fiji (National Institutes of Health)[87] and/or Bitplane Imaris.

Analysis of endogenous mesendoderm cell internalization

The Imaris Spot plugin was used to track individual internalizing cells in vivo. Internalization onset (0 min) was defined as the time point immediately before a clear shift in the Z position of mesendoderm cells at the blastoderm margin became clearly detectable. At 0 min, 40 cells, at varying distances from the blastoderm margin, were selected and tracked for 60 min in 3D confocal stacks, including through cell division events. For wt embryos, this tracking was extended up to 90 min after internalization onset. Reference spots were added manually at the blastoderm margin, so that all embryos could be rotated into a similar orientation. The position of all tracked cells as a function of time was then exported into an Excel sheet and processed using a custom-made code.

To calculate the correlation between initial (0 min) and final position (60 min), the relative cell position x_i (resp. x_f) along the $\tilde{x}$ axis pre- and post-internalization was normalized so that $x = 0$ refers to the cell closest to the margin and $x = 1$ to the cell furthest away from it. When a cell divided, x_f was defined as the average coordinate of its daughters at 60 min. For this analysis, we considered only cells that had started to internalize by 60 min, defined as any cell that moved by at least 15 μm towards the YSL. Thus, for ordered tissue internalization (where the first internalized cells at 0 min should have migrated furthest away from the margin by 60 min), x_i and x_f would be perfectly anti-correlated ($1 - x$ slope; Fig. 1f, dashed line, for example). The correlation analysis between 60 and 90 min was performed in the same way, although in this case, as this analysis was performed on cells that had already internalized by 60 min, perfect order entailed a perfect correlation between x_i and x_f (x slope; Fig. 5b, dashed line, for example).

To determine the time of internalization onset, the temporal evolution of the $z_j(t)$ coordinate for each cell j (that is, how much a cell moves towards the YSL) was best-fitted by the simple logistic function

$$z_{\mathrm{fit}}(t) = z_0 + \frac{z_f - z_0}{1 + e^{-\frac{t-T}{\tau}}},$$

where z_0 and z_f are fitting parameters denoting the initial (z_0) and final (z_f) position, T is the time at which the internalization dynamics is maximum and τ is the characteristic duration of cell internalization. $t_{\mathrm{in}} = T - 2\tau$ was then defined as the internalization onset for a given

cell j and correlated to its initial distance δx_j to the margin in the x direction at $t = 0$.

Finally, the average distance by which a cell moved in the z direction ($z_j(t) - z_j(t = 0)$ for t = 15, 30, 45 and 60 min) was also quantified independently of any fitting procedure and correlated to its initial distance δx_j to the margin at $t = 0$. This initial distance to the margin δx_j was then binned according to the average cell size, determined as the average cell height of 20 cells per embryo during early stages of tissue internalization.

Analysis of mesendoderm donor cell internalization

The Spot plugin of Imaris was used to obtain the initial number and coordinates of donor cell nuclei, as well as reference landmarks at the deep cell margin. Using a custom-made MATLAB code[39], all nuclei and reference landmarks were projected along the Z axis. The geometrical distance of the projected nuclei to the closest reference spot was then automatically calculated and exported into an output Excel sheet. Only donor cells placed within 150 μm to the blastoderm margin of MZ*oep* host embryos were considered for subsequent analysis. A few additional criteria were considered for this analysis, namely (i) donor cell integrity must be preserved, at least, until host embryos reached 100% epiboly, and (ii) donor cells must express comparable levels of EGFP-CAAX or EGFP within a transplanted cluster, in Tg(*gsc::EGFP-CAAX*) or Tg(*mezzo::EGFP*) embryos, respectively, to exclude cases where ectoderm or EVL cells, or yolk granules, were co-transplanted with mesendoderm cells. Similar exclusion criteria were employed for all transplantation assays included in this study.

Using the same spot function aided by cross-section projections, the total number of transplanted cells and the number of donor cells which arrived at the YSL were determined as a function of the developmental stage of the host embryo to normalize the data across embryos. To determine the host developmental stage, the Imaris Measurement tool was used to quantify the total embryo length and the length covered by the deep cells at any given time point. This measurement was performed in a single-plane image at the bottom of the imaged volume, to be as close as possible to the centre of the embryo, and then calculated as the percentage of deep cell epiboly.

Analysis of mesendoderm cell protrusiveness

The multi-point tool of Fiji was used to obtain the coordinates at the base of each cell protrusion and at its tip. Using these vectors (base to tip), the orientation and length of cell protrusions were then calculated by translating the vectors to spherical coordinates (r, θ, ϕ) using the classical physics convention.

$$\text{Cell protrusion length}, r = \sqrt{x^2 + y^2 + z^2},$$

$$\text{Angle}, \theta = \arctan\left(\frac{\sqrt{x^2 + y^2}}{z}\right).$$

The angle θ quantifies the orientation of protrusions along the EVL–YSL axis. Protrusions are oriented exactly towards the EVL when $\theta = \pi$ or towards the YSL when $\theta = 0$. F-actin-positive extensions exhibiting dynamic behaviour (appearance and eventual retraction) and blebs, defined as dynamic membrane extensions devoid of an F-actin-rich cortex, were included in the analysis. We restrained from further categorization of these cellular protrusions owing to the complex 3D environment in vivo. Cell protrusions were analysed in 3D confocal stacks every 5 min for 1 h, either upon cell transplantation or within the intact embryo. The total number of measured cell protrusions was divided by the number of analysed cells to obtain the number of protrusions per cell (the instantaneous analysis is also shown in Extended Data Figs. 2b–d and 6f,g). Mesendoderm cell protrusion

number, length and orientation were averaged across time points and experimental replicates.

To relate cell protrusiveness to the internalization competence of mesendoderm cells, cell protrusions were analysed for the first hour after the start of acquisition and the number of donor cells which arrived at the YSL was determined 4 h later. Since these embryos were imaged at higher magnification, their exact developmental stage 4 h after the start of acquisition could not be determined, but it likely corresponded to 90–100% epiboly stage. These transplantation assays were repeated and imaged at lower resolution, confirming our observations in the high-magnification videos (Extended Data Figs. 2h–j' and 3g–j).

To analyse endogenous mesendoderm protrusiveness, two time windows, that is early (0–60 min) and late (60–120 min), were defined to compare protrusion number, length and orientation. Internalization onset (0 min) was defined as described for the cell tracking analysis above. This temporal subdivision was chosen to compare the protrusiveness of 'leaders' versus 'followers' and corresponded approximately to the time difference between 50% epiboly and mid-to-late shield stage in the transplantation assays (Extended Data Fig. 1a). For each temporal window, 3–5 cells were initially selected per embryo, and both daughter cells were analysed in case of cell division.

Analysis of mesendoderm donor cell sphericity
The Surface plugin of Imaris was used to automatically segment the surface of the transplanted mesendoderm cell clusters, based on their EGFP-CAAX expression in Tg(*gsc::EGFP-CAAX*) embryos, and output their sphericity values (defined as $\pi^{\frac{1}{3}}(6 \times \text{volume})^{\frac{2}{3}}/\text{area}$, so that a perfect sphere would have a sphericity of 1). In cases where the *gsc::EGFP-CAAX* expression/intensity was low and therefore incompatible with high-quality automatic segmentation, the outline of the cell clusters was determined manually using the draw tool of the Surface plugin. The analysis was restricted to mesendoderm cell clusters (composed of, at least, two donor cells) and, when there was more than one transplanted donor cell cluster, the same analysis was performed for each individual cluster and averaged per transplant for the analysis shown in Extended Data Fig. 5b,f,j' and, subsequently, averaged across all transplants for the analysis shown in Extended Data Fig. 5j.

Analysis of pSmad2/3 nuclear localization
Analysis of the nuclear accumulation of pSmad2/3 was performed as described previously[39]. In short, the Spot plugin of Imaris was used to obtain the 3D coordinates of all cell nuclei, as well as reference landmarks at the deep cell margin. The nuclei of EVL cells, cells undergoing division, and cells displaying low-intensity DAPI-positive nuclei were manually excluded from the subsequent analysis. The remaining nuclei were filtered for (i) Z position, to restrict the analysis to the top 100 μm and avoid depth-related intensity changes, and (ii) maximum fluorescence intensity below 65,536 grey values, to avoid oversaturated pixels. For shield and 75% epiboly stage embryos, the analysis was manually restricted to non-internalized progenitors. Using a custom-made MATLAB code[39], the nuclei were projected along the Z axis and the geometrical distance of projected nuclei to the closest reference spot was then automatically calculated and exported along with their mean fluorescence intensity for pSmad2/3 and DAPI channels. For background subtraction, 15 spots were manually added within the cytoplasm of cells located at the bottom of the imaged volume. To try to correct depth-related artefacts, the ratio between the mean fluorescence intensities for nuclear pSmad2/3 and DAPI was calculated (normalized pSmad2/3 intensity), after background subtraction for both channels.

To plot the distance of a given nuclei to the blastoderm margin as cell tiers, we first measured the average size of 10–15 cells per wt embryo at different stages of gastrulation. For each stage, we then subtracted the minimum distance obtained between any nuclei and the reference spots and binned the data according to the measured cell size. The normalized intensity of nuclear pSmad2/3 as a function of their distance to the margin was then averaged across experimental replicates.

Analysis of E-Cad levels at cell−cell contacts
As a proxy for overall E-Cad expression levels in *control* and *e-cad* morphant embryos, the mean fluorescence intensity at 30 cell−cell contacts per embryo was measured using the line tool in Fiji (two pixels thick line at similar Z position, to avoid depth-related artefacts). To avoid quantifying non-specific signal, the mean fluorescence intensity within the cytosol of five or six cells was also measured and then subtracted to the values obtained at the cell−cell contacts.

Analysis of heterotypic donor cell clusters
To analyse the cohesion of heterotypic clusters after transplantation, the initial composition of the cluster and distance of all donor cells to the blastoderm margin were determined as described above. By the end of epiboly in host embryos, the Spot plugin of Imaris was used to quantify the total number of 'late' mesendoderm donor cells (shield, 75% epiboly or shield+75% epiboly) that remained clustered with 'early' cells (50% epiboly). For heterotypic clusters composed of donor mesendoderm cells collected from 50% and shield stage embryos, which tend to remain cohesive by the end of host embryo epiboly (Extended Data Fig. 6a), the proportion of shield cells which had arrived at the YSL was also quantified as described above (Fig. 3e,f). In cases where heterotypic clusters (partially or completely) split, the type of cell−cell contact (homotypic versus heterotypic) lost upon cluster splitting was recorded. A contact loss within the transplanted cluster was defined as a splitting event in case the split lasted more than two consecutive frames (approximately 10–15 min).

Statistics
The statistical analyses and plots were performed using Microsoft Excel, Gnuplot and/or GraphPad Prism. The number of transplants or embryos (n) and experimental replicates (N) analysed are indicated in the figure legends. At least three independent experiments were performed in all cases, except for the *sox17* in situ hybridization shown in Extended Data Fig. 3b, where only two independent experiments were conducted. Error bars are indicated in the figures. No statistical test was performed to determine the sample sizes. The statistical tests used to assess significance are indicated in the figure legends, along with the corresponding P values. To choose an appropriate statistical test, the distribution of each group was first analysed using the D'Agostino–Pearson normality test. To compare two groups, a two-sided t test or a Mann–Whitney test was used, depending on whether either data set shows normal distribution. In cases where a t-test was used, the variances were subsequently tested using the F-test. To compare more than two groups, either analysis of variance or Kruskal–Wallis test was performed, depending on whether all groups show normal distribution. To increase statistical power, a correction for multiple comparisons was used in these cases.

Reporting summary
Further information on research design is available in the Nature Research Reporting Summary linked to this article.

Data availability
Source data are available for this paper. All other data that support the plots within this manuscript and other findings of this study are available from the corresponding author upon reasonable request. Source data are provided with this paper.

Code availability
Code is available for this paper at https://doi.org/10.1038/s41567-022-01787-6.

References

73. Westerfield, M. *The Zebrafish Book. A Guide for the Laboratory Use of Zebrafish (Danio rerio)* (Univ. of Oregon Press, 2000).
74. Smutny, M. et al. Friction forces position the neural anlage. *Nat. Cell Biol*. **19**, 306–317 (2017).
75. Ruprecht, V. et al. Cortical contractility triggers a stochastic switch to fast amoeboid cell motility. *Cell* **160**, 673–685 (2015).
76. Kimmel, C. B., Ballard, W. W., Kimmel, S. R., Ullmann, B. & Schilling, T. F. Stages of embryonic development of the zebrafish. *Dev. Dyn*. **203**, 253–310 (1995).
77. Villefranc, J. A., Amigo, J. & Lawson, N. D. Gateway compatible vectors for analysis of gene function in the zebrafish. *Dev. Dyn*. **236**, 3077–3087 (2007).
78. Ridley, A. J., Paterson, H. F., Johnston, C. L., Diekmann, D. & Hall, A. The small GTP-binding protein rac regulates growth factor-induced membrane ruffling. *Cell* **70**, 401–410 (1992).
79. Hall, A. Rho GTpases and the actin cytoskeleton. *Science* **279**, 509–514 (1998).
80. Arboleda-Estudillo, Y. et al. Movement directionality in collective migration of germ layer progenitors. *Curr. Biol*. **20**, 161–169 (2010).
81. Iioka, H., Ueno, N. & Kinoshita, N. Essential role of MARCKS in cortical actin dynamics during gastrulation movements. *J. Cell Biol*. **164**, 169–174 (2004).
82. Behrndt, M. et al. Forces driving epithelial spreading in zebrafish gastrulation. *Sci. (80-.)*. **338**, 257–260 (2012).
83. Rebagliati, M. R., Toyama, R., Haffter, P. & Dawid, I. B. cyclops encodes a nodal-related factor involved in midline signaling. *Proc. Natl Acad. Sci. U. S. A*. **95**, 9932–9937 (2002).
84. Soh, G. H., Pomreinke, A. P. & Müller, P. Integration of Nodal and BMP signaling by mutual signaling effector antagonism. *Cell Rep*. **31**, 107487 (2020).
85. Schwayer, C. et al. Mechanosensation of Tight Junctions Depends on ZO-1 Phase Separation and Flow. *Cell* **179**, e18 (2019).
86. Thisse, C. & Thisse, B. High-resolution in situ hybridization to whole-mount zebrafish embryos. *Nat. Protoc*. **3**, 59–69 (2008).
87. Schindelin, J. et al. Fiji: An open-source platform for biological-image analysis. *Nat. Methods* **9**, 676–682 (2012).

Author contributions

D.P., É.H. and C.-P.H. designed the research. D.P. performed the experiments and analysed the experimental data. R.K. created the DN-Rac1 plasmid. É.H. developed the numerical simulations and analysed the experimental data. D.P. and C.-P.H. wrote the manuscript with input from all authors.

Competing interests

The authors declare no competing interests.

Additional information

Extended data is available for this paper at https://doi.org/10.1038/s41567-022-01787-6.

Supplementary information The online version contains supplementary material available at https://doi.org/10.1038/s41567-022-01787-6.
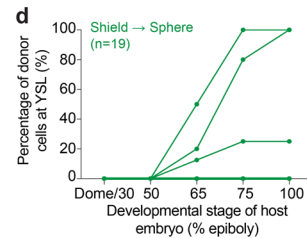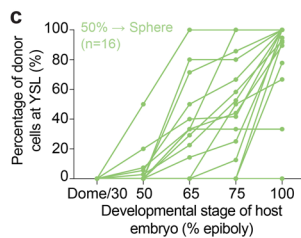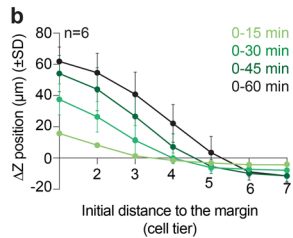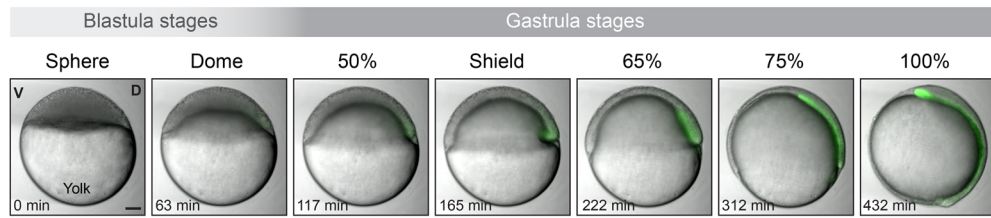
Correspondence and requests for materials should be addressed to Édouard Hannezo or Carl-Philipp Heisenberg.

Peer review information *Nature Physics* thanks M. Lisa Manning, Patrick Mueller and the other, anonymous, reviewer(s) for their contribution to the peer review of this work.

**Reprints and permissions information** is available at www.nature.com/reprints.
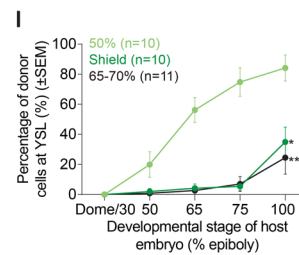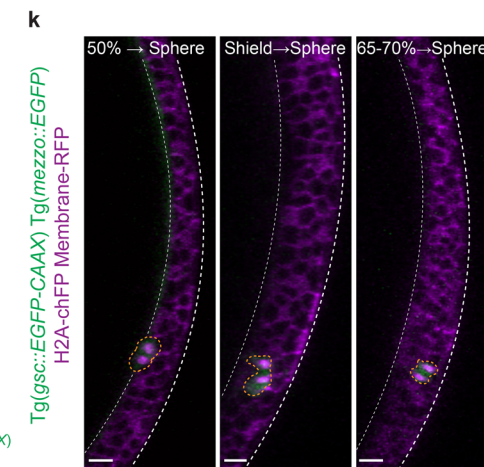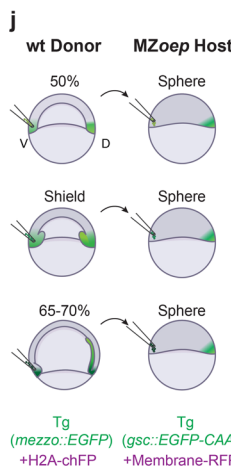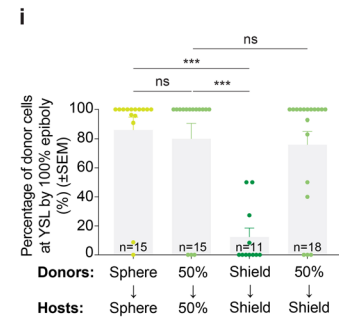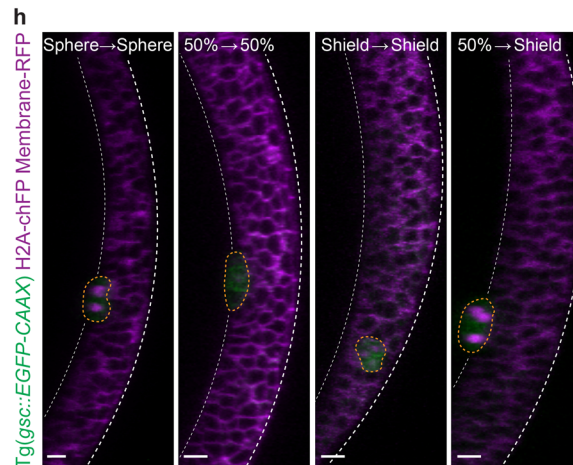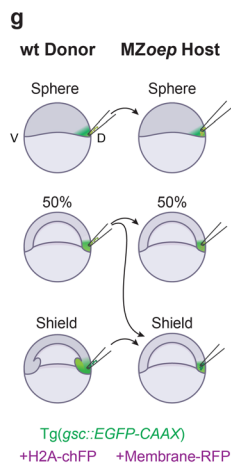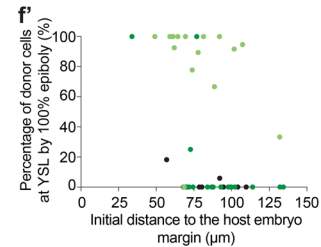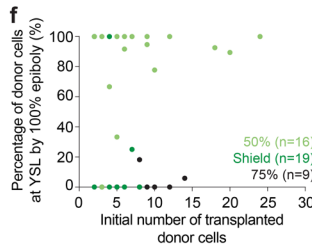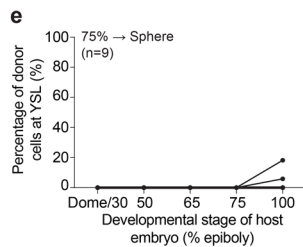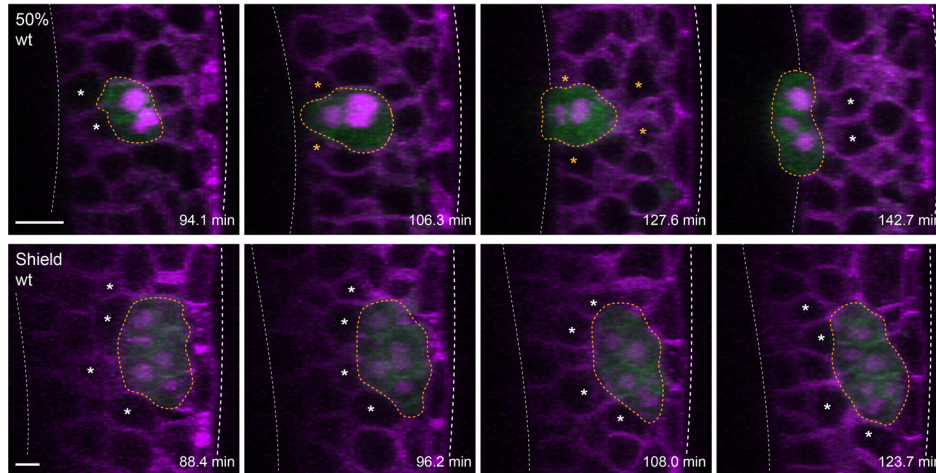
Extended Data Fig. 1 | See next page for caption.

Extended Data Fig. 1 | Loss of internalization capacity of mesendoderm cells is cell-autonomous. (a) Bright-field single-plane images of a gastrulating embryo expressing *gsc::EGFP-CAAX* (green), marking axial mesendoderm cells. **(b)** Change in Z position, a proxy for cell internalization, of mesendoderm cells as a function of their initial distance to the margin in wt embryos (N = 6). Colour-code corresponds to distinct time bins. **(c-f')** Percentage of internalized mesendoderm donor cells, collected from 50% (c, N = 9), shield (d, N = 12) or 75% epiboly (e, N = 8) stage embryos, as a function of the host developmental stage (c-e), the initial number of transplanted cells (f) or the initial distance of the transplanted cells to the host margin (f'). **(g)** Schematic representation of the mesendoderm cell transplants in (h). **(h)** High-resolution confocal images of transplanted mesendoderm donor cells, collected from sphere, 50% or shield stage embryos, by the end of host embryo epiboly. Donor cells are marked by *gsc::EGFP-CAAX* (green) and H2A-chFP expression (magenta, nuclei). MZ*oep* hosts express low levels of *gsc::EGFP-CAAX* (green) and Membrane-RFP (magenta). Developmental stage of donors/hosts is indicated in the top. Dashed white lines indicate EVL and YSL. Yellow dashed lines outline the donor cells.

(i) Percentage of internalized mesendoderm donor cells, collected from sphere, 50% or shield stage embryos, by the end of host embryo epiboly. Developmental stage of donors/hosts is indicated below (sphere→sphere: N = 6; 50%→50%: N = 5; shield→shield: N = 7; 50%→shield: N = 7). **(j)** Schematic representation of the heterochronic transplants in (k). **(k)** High-resolution confocal images of transplanted mesendoderm donor cells, collected from the ventral blastoderm margin of 50%, shield or 65–70% epiboly stage embryos, by the end of host embryo epiboly. Donor cells are marked by *mezzo::EGFP* (green) and H2A-chFP expression (magenta, nuclei). MZ*oep* hosts and dashed lines as in (h). **(l)** Percentage of internalized donor mesendoderm cells, collected from 50% (N = 4), shield (N = 6) or 65–70% epiboly (N = 5) stage embryos, as a function of the host embryo developmental stage. Data are shown as mean ± SEM. Kruskal-Wallis test. NS: Not significant, ***P = 0.0004 (sphere→sphere versus shield→shield), ***P = 0.0003 (50%→50% versus shield→shield) (i). *P = 0.167, **P = 0.0022 (l) (i, l). Lateral view (a), Dorsal view (cross-section: (h, k). D: dorsal; V: ventral. Scale bars: 100 μm (a), 20 μm (h, k).
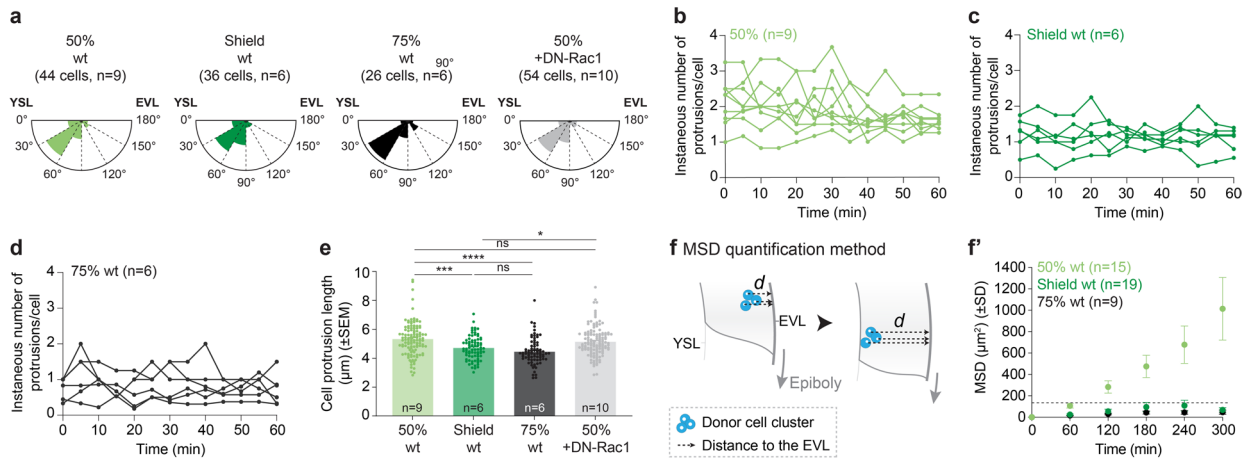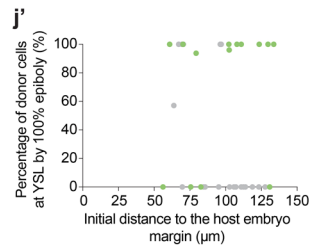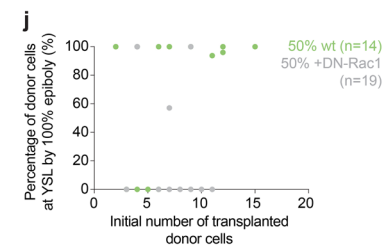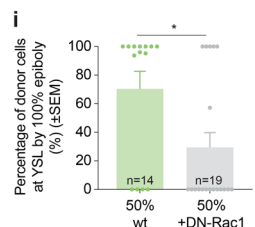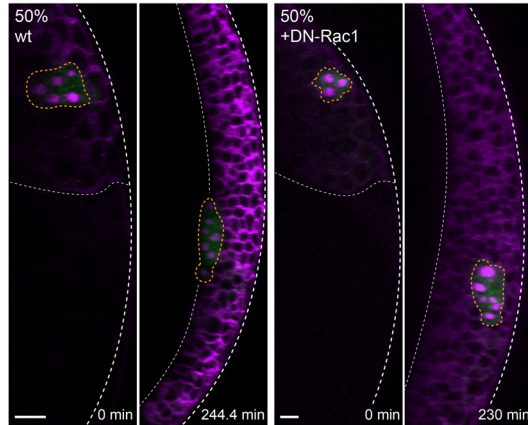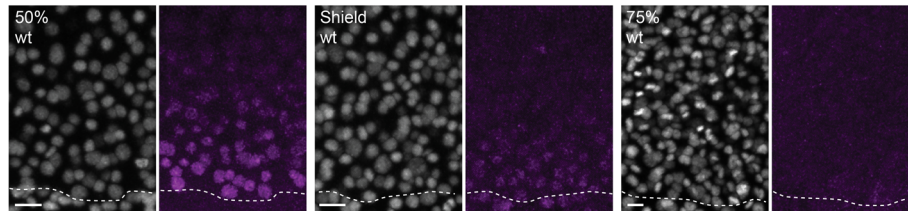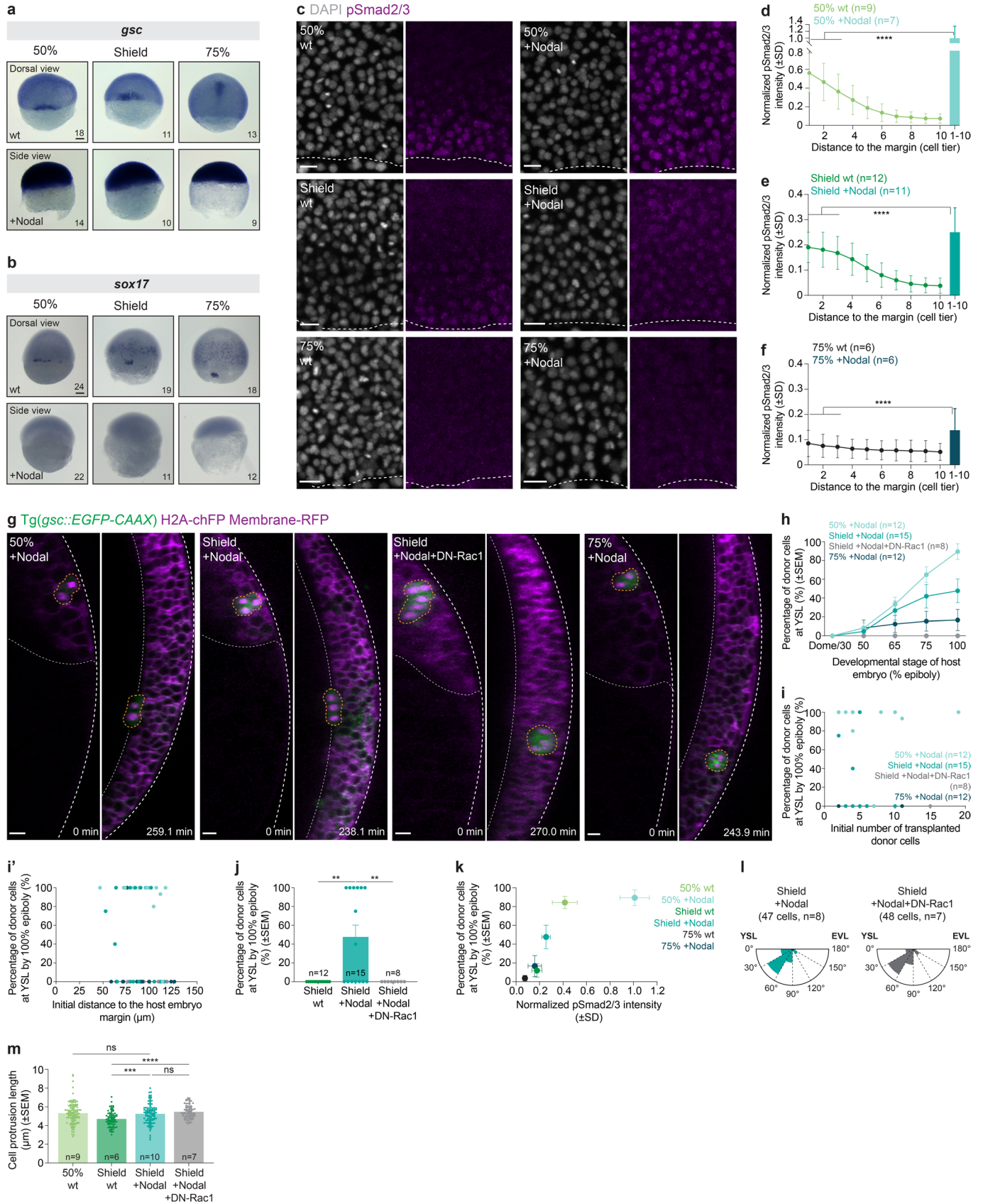
Extended Data Fig. 2 | See next page for caption.

Extended Data Fig. 2 | Internalization-incompetent mesendoderm donor cells exhibit caged motion. (a) Rose plot of cell protrusion orientation in transplanted wt or DN-Rac1-overexpressing mesendoderm donor cells, collected from 50% (wt: N = 7; +DN-Rac1: N = 10), shield (wt: N = 4) or 75% epiboly stage (wt: N = 5) embryos. **(b-d)** Instantaneous number of protrusions formed per transplanted mesendoderm donor cell, collected from 50% (b, 44 cells, N = 7), shield (c, wt: 36 cells, N = 4) or 75% epiboly stage (d, wt: 26 cells, N = 5) embryos. Each curve corresponds to a transplanted cluster. **(e)** Length of protrusions formed by transplanted mesendoderm donor cells, collected from wt or DN-Rac1-overexpressing donor embryos at 50% (wt: 44 cells, N = 7; +DN-Rac1: 54 cells, N = 10), shield (wt: 36 cells, N = 4) or 75% epiboly stage (wt: 26 cells, N = 5). Each dot corresponds to the average length of cell protrusions in a transplant at a given time point. **(f)** Schematic representation of the quantification strategy to measure the distance travelled by the donor cells along the internalization axis, used to calculate the MSD shown in (f'). **(f')** Mean squared relative displacement (MSD) of transplanted mesendoderm donor cells, collected from 50% (N = 9), shield (N = 12) or 75% epiboly stage (N = 8) embryos. Dashed line corresponds to the average cell size at 300 min (see also Fig. 1i for the percentage of internalized donor cells and Supplementary Note). **(g)** High-resolution confocal images of transplanted mesendoderm donor cells, collected from 50% epiboly or shield stage embryos (also provided as Supplementary Video 3). Donor cells are marked by *gsc::EGFP-CAAX* (green) and H2A-chFP expression (magenta, nuclei).

MZ*oep* hosts express low levels of *gsc::EGFP-CAAX* (green) and Membrane-RFP (magenta). Dashed white lines outline EVL and YSL. Yellow dashed lines outline the donor cell clusters. White asterisks denote neighbouring host cells and yellow asterisks mark neighbouring host cells that had lost contact and/or will regain it in subsequent timepoints. **(h)** High-resolution confocal images of transplanted control or DN-Rac1-overexpressing mesendoderm donor cells, collected from 50% epiboly embryos. Donor cells, host embryos and dashed lines as in (g). For each transplant, the first acquired time point and the time point when the hosts reached 100% epiboly are shown. **(i)** Percentage of internalized control or DN-Rac1-overexpressing mesendoderm donor cells, collected from 50% epiboly embryos (N = 9), by the end of host embryo epiboly. **(j, j')** Percentage of internalized control or DN-Rac1-overexpressing mesendoderm donor cells, collected from 50% epiboly embryos, as a function of the initial number of transplanted cells (g; N = 9) or the initial distance of the transplanted cells to the host embryo margin (g'; N = 9). **(k)** High-resolution confocal images of wt embryos stained for DAPI (grey, nuclei) and pSmad2/3 (magenta) at 50%, shield and 75% epiboly stage (see also Fig. 2d). Dashed lines indicate deep cell margin. Data are shown as mean ± SEM (e, i) or SD (f'). Kruskal-Wallis test. NS: not significant. ****P = < 0.0001, ***P = 0.0004, *P = 0.0188 (e). t test (two-sided). *P = 0.0153 (i). Dorsal view (cross-section: (g, h), top view: (k)). Scale bars: 10 μm (g), 20 μm (h, k).

Extended Data Fig. 3 | See next page for caption.

Extended Data Fig. 3 | Increasing Nodal signalling in late mesendoderm cells prolongs their internalization capacity. (a, b) Expression of mesendoderm marker genes (*gsc* (a, N = 3) and *sox17* (b, N = 2)) as determined by in situ hybridization of wt and Nodal-overexpressing embryos at different stages of gastrulation. Number of embryos is in the lower corner. **(c)** High-resolution confocal images of wt and Nodal-overexpressing embryos stained for DAPI (grey, nuclei) and pSmad2/3 (magenta) at 50%, shield and 75% epiboly stage. Dashed lines indicate deep cell margin. **(d-f)** Normalized intensity of nuclear pSmad2/3 as a function of their distance to the blastoderm margin in wt and Nodal-overexpressing embryos at 50% (d, N = 4), shield (e, N = 4) and 75% epiboly (f, N = 3) stage. **(g)** High-resolution confocal images of transplanted Nodal-overexpressing donor cells, collected from control or DN-Rac1-expressing embryos at 50%, shield and 75% epiboly stage embryos. Donor cells are marked by *gsc::EGFP-CAAX* (green) and H2A-chFP expression (magenta, nuclei). MZ*oep* hosts express low levels of *gsc::EGFP-CAAX* (green) and Membrane-RFP (magenta). For each transplant, the first acquired time point and the time point when hosts reached 100% epiboly are shown. Dashed white lines indicate EVL and YSL. Yellow dashed lines outline donor cell transplants. **(h-i')** Percentage of internalized Nodal-overexpressing donor cells, collected from wt or DN-Rac1-expressing embryos at 50% (N = 5), shield (+Nodal: N = 7, +DN-Rac1: N = 3) or 75% epiboly (N = 6) stage embryos, as a function of the host embryo developmental stage (h), the initial number of transplanted cells (i) or the initial distance of the transplanted cells to the host embryo margin (i'). **(j)** Percentage of internalized control and DN-Rac1-expressing donor cells, collected from

wt or Nodal-overexpressing embryos at shield (control: N = 8, +Nodal: N = 7, +Nodal+DN-Rac1: N = 3) stage embryos, by the end of host embryo epiboly (data for all Nodal-overexpressing cells are also shown (h)). **(k)** Percentage of internalized wt and Nodal-overexpressing donor cells, collected from 50%, shield or 75% epiboly stage embryos, as a function of the normalized intensity of nuclear pSmad2/3, averaged over the first 3 cell tiers for wt embryos and over the first 10 cell tiers for Nodal-overexpressing embryos (to account for the steep Nodal gradient observed at the blastoderm margin of wt embryos and the homogeneous nuclear accumulation of pSmad2/3 observed in Nodal-overexpressing embryos; the data are also shown in Figs. 1i, 2e and in (d-f, h). **(l)** Rose plot of cell protrusion orientation in transplanted mesendoderm donor cells overexpressing Nodal, alone or in combination with DN-Rac1, collected from shield stage embryos (+Nodal: N = 5; +Nodal+DN-Rac1: N = 7). **(m)** Length of protrusions formed by transplanted donor cells, collected from wt and Nodal-overexpressing embryos control or co-expressing DN-Rac1, at 50% epiboly (wt: 44 cells, N = 7) or shield stage (wt: 36 cells, N = 4; +Nodal: 47 cells, N = 5; +Nodal+DN-Rac1: 48 cells, N = 7; wt data are shown in Extended Data Fig. 2e). Each dot in the graph corresponds to the average length of cell protrusions in a single transplant at a given time point. Data are shown as mean ± SD (d-f, k) or SEM (h, j, k, m). Mann-Whitney test (two-sided). ****P < 0.0001 (d-f). Kruskal-Wallis test. **P = 0.0026 (shield wt versus shield +Nodal), **P = 0.0090 (shield + Nodal versus shield +Nodal+DN-Rac1) (j). NS: not significant. ****P < 0.0001. ***P = 0.0003 (l), (j, l). Side view (a, b); Dorsal view (top view: (a, b, c); cross-section: (g)). Scale bars: 100 μm (a, b), 20 μm (c, g).
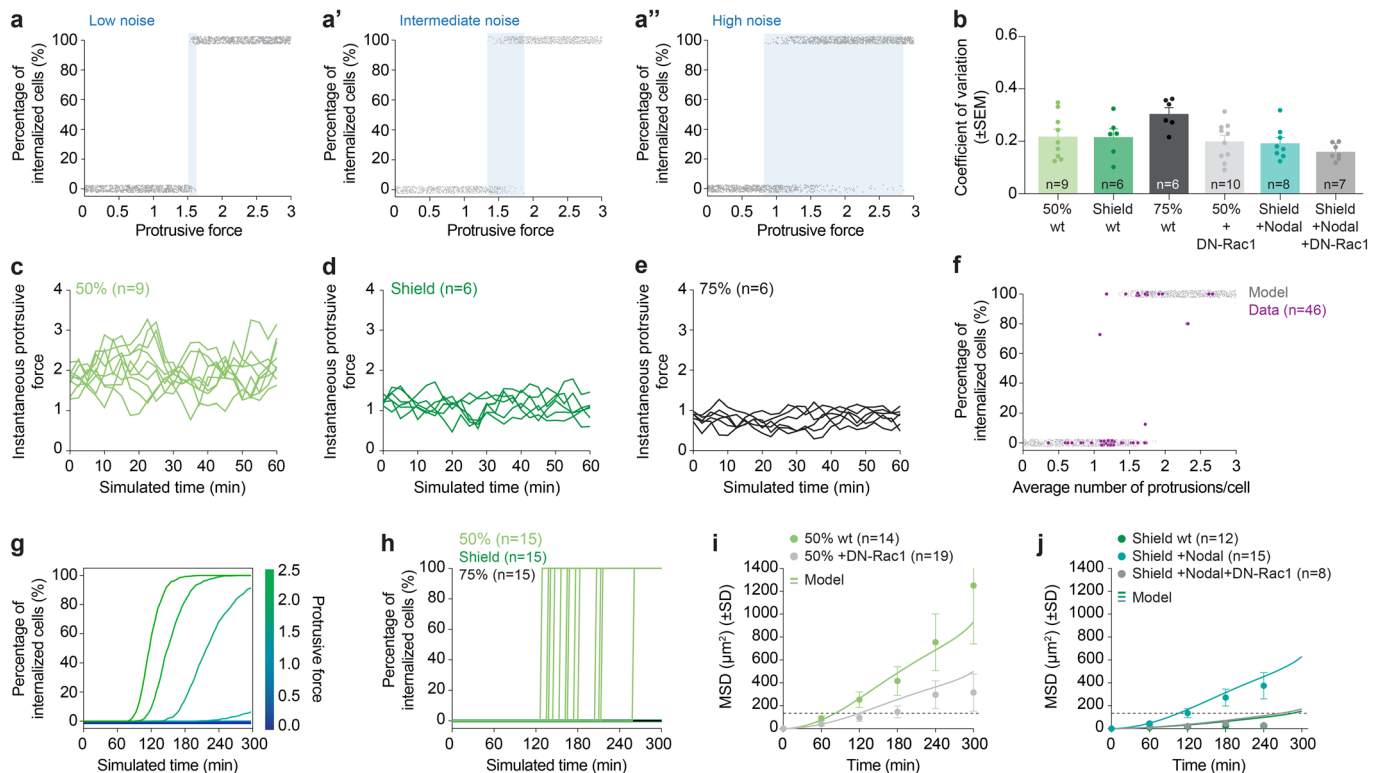
**Extended Data Fig. 4 | Motility-driven (un)jamming underlies the transition between mesendoderm leaders and follower cells. (a-a")** Prediction from the toy-model of motility-driven (un)jamming for the relationship between internalization capacity and average protrusive force F for different values of noise σ, respectively 5% (a), 20% (a') or 100% (a") normalized standard deviation in the protrusive force (see Supplementary Note). Each dot represents a simulation outcome (dispersion along the y axis was added to better convey the probability associated with a given internalization outcome as a function of F). Increasing noise σ in the protrusive force F results in a progressive increase of the bistable region (blue shaded interval), where for the same value of average protrusive force, cells can either internalize or stay out. **(b)** Coefficient of variation for the number of protrusions formed by control or DN-Rac1-expressing mesendoderm cells, collected from wt and Nodal-overexpressing embryos at 50% (wt: 44 cells, N = 7; +DN-Rac1: 54 cells, N = 10), shield (wt: 36 cells, N = 4; +Nodal: 47 cells, N = 5; +Nodal+DN-Rac1: 48 cells, N = 7) or 75% epiboly (wt: 26 cells, N = 5) stage, upon transplantation. **(c-e)** Instantaneous protrusive forces for simulated cell clusters for average protrusive force $F = 1.86$ (c), $F = 1.15$ (d) and $F = 0.83$ (e), corresponding to the average number of protrusions formed by mesendoderm donor cells from 50%, shield or 75% epiboly stage embryos, respectively (see Fig. 2b and Extended Data Fig. 2b–d for the experimental data). **(f)** Percentage of internalized cells as a function of the average number of protrusions formed per cell across all experimental conditions (purple, each

dot represents a single transplant; average data shown in Fig. 3b) and predicted by the model (grey, same parameters as (a')). **(g)** Percentage of internalized cells as a function of time in the numerical simulations (same parameters as (a')) for different values of protrusive force F, respectively $F = 0.35, 0.7, 1.05, 1.75, 2.1, 2.45$. **(h)** Percentage of internalized cells as a function of time in individual simulations for protrusive force $F = 1.86$ (light green), $F = 1.15$ (dark green) and $F = 0.83$ (black), corresponding to the average number of protrusions formed by mesendoderm donor cells collected from 50%, shield or 75% epiboly stage embryos, respectively (see Fig. 2b). For $F = 1.15$ and $F = 0.83$, we found no internalization events occur, while for $F = 1.86$ internalization is robust, but highly asynchronous, mirroring the experimental findings shown in Extended Data Fig. 1c. **(i)** Mean squared relative displacement (MSD) of control or DN-Rac1-expressing donor cells, collected from 50% epiboly (N = 9) stage embryos upon transplantation, and predicted by the model based on their experimentally measured average protrusiveness. The dashed line corresponds to the average cell size at 300 min (see also Extended Data Fig. 2i for the percentage of internalized cells and Supplementary Note). **(j)** MSD of control or Nodal-overexpressing donor cells, collected from wt or DN-Rac1-expressing shield stage embryos (wt: N = 8, +Nodal: N = 7, +Nodal+DN-Rac1: N = 3) upon transplantation, and predicted by the model based on their experimentally measured average protrusiveness. Dashed line as in (i; see also Extended Data Fig. 3j for the percentage of internalized cells and Supplementary Note for details). Data are shown as mean ± SEM (b) or SD (i, j).
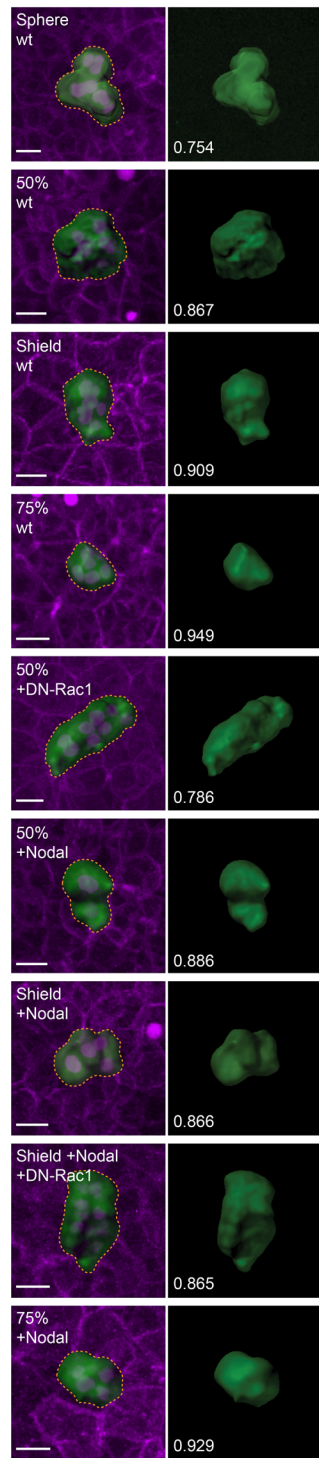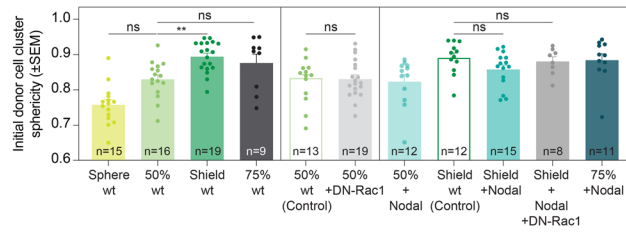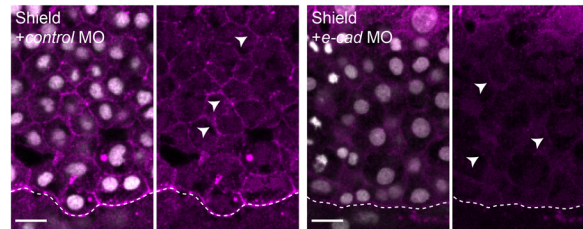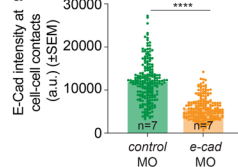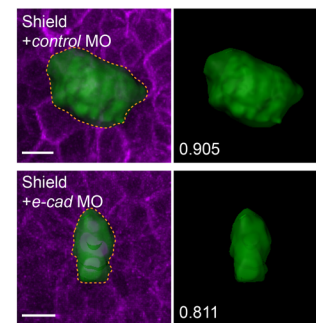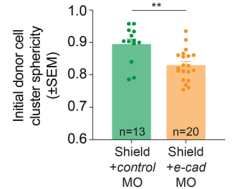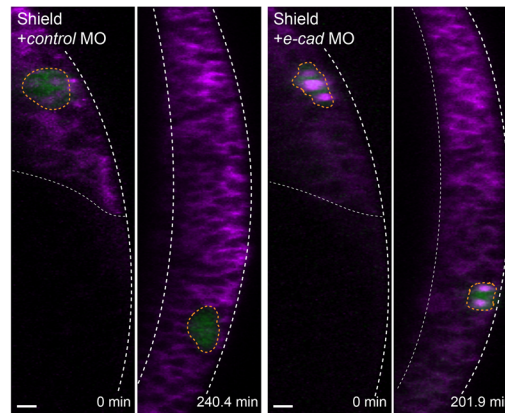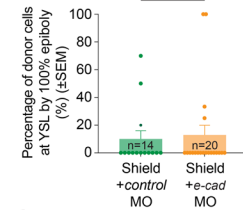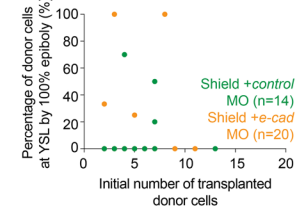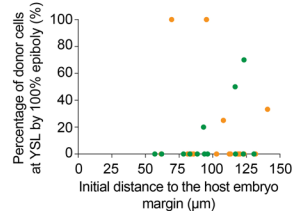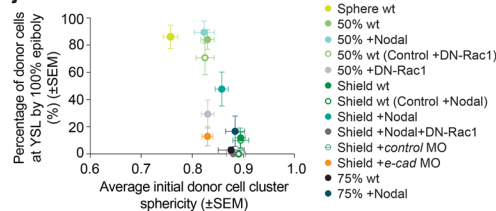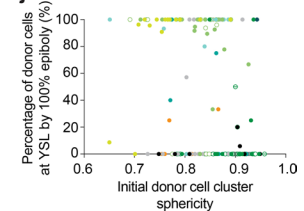
Extended Data Fig. 5 | See next page for caption.

Extended Data Fig. 5 | Reducing cell-cell adhesion is not sufficient to rescue the loss of internalization capacity of late mesendoderm cells. (a) High-resolution confocal images of transplanted control or DN-Rac1-expressing mesendoderm cells, collected from wt and Nodal-overexpressing embryos at sphere, 50%, shield or 75% epiboly stage embryos. Donor cells are marked by *gsc::EGFP-CAAX* (not shown) and H2A-chFP expression (magenta, nuclei). MZ*oep* hosts express low levels of *gsc::EGFP-CAAX* (not shown) and Membrane-RFP (magenta). The surface of the donor clusters is shown in green and the corresponding sphericity values are indicated in the bottom left corner. Yellow dashed lines outline donor cell transplants. These segmented clusters were also shown in Fig. 1h, Extended Data Fig. 1h (left panel), Extended Data Fig. 2h and Extended Data Fig. 3g to allow for a direct comparison between changes in mesendoderm cluster cell compaction and internalization outcomes. **(b)** Initial donor cell cluster sphericity of transplanted control or DN-Rac1-expressing mesendoderm cells, collected from wt and Nodal-overexpressing embryos at sphere (wt: N = 6), 50% (wt: N = 9, wt (+DN-Rac1 control): N = 9, +DN-Rac1: N = 9, +Nodal: N = 5), shield (wt: N = 12, wt (+Nodal control): N = 8, +Nodal: N = 7, +Nodal+DN-Rac1: N = 3) or 75% epiboly (wt: N = 8, +Nodal: N = 6) stage embryos. **(c)** High-resolution confocal images of *control* or *e-cad* MO-injected embryos immunostained for DAPI (grey, nuclei) and E-Cad (magenta) at shield stage. Morphant embryos were co-injected with H2B-GFP (not shown) to select for homogeneously-injected embryos. **(d)** Intensity of E-Cad at cell-cell contacts in *control* or *e-cad* MO-injected embryos at shield stage (N = 3). **(e)** High-resolution confocal images of transplanted mesendoderm donor cells, collected from *control* or *e-cad* MO-injected embryos at shield stage. Donor cells, host embryos, the surface of the donor cell clusters, sphericity values and yellow dashed lines as in (a; also shown in (g)). **(f)** Initial donor cell cluster sphericity of transplanted

mesendoderm donor cells clusters, collected from *control* (N = 7) or *e-cad* MO (N = 6)-injected embryos at shield stage. **(g)** High-resolution confocal images of transplanted mesendoderm donor cells, collected from *control* or *e-cad* MO-injected embryos at shield stage. Donor cells are marked by *gsc::EGFP-CAAX* (green) and H2A-chFP expression (magenta, nuclei). MZ*oep* hosts express low levels of *gsc::EGFP-CAAX* (green) and Membrane-RFP (magenta). For each transplant, the first acquired time point and the time point when hosts reached 100% epiboly are shown. Dashed white lines indicate EVL and YSL. Yellow dashed lines as in (a). **(h)** Percentage of internalized mesendoderm donor cells, collected from *control* (N = 7) or *e-cad* MO (N = 6)-injected embryos at shield stage, by the end of host embryo epiboly. **(i, i')** Percentage of internalized mesendoderm donor cells, collected from *control* (N = 7) or *e-cad* MO (N = 6)-injected embryos at shield stage, as a function of the initial number of transplanted cells (i) or the initial distance of the transplanted cells to the host embryo margin (i'). **(j, j')** Percentage of internalized control or DN-Rac1-expressing mesendoderm donor cells, collected from wt, Nodal-overexpressing or *e-cad* MO-injected embryos at sphere (wt: n = 15, N = 6), 50% (wt: n = 16, N = 9; wt (+DN-Rac1 control): n = 14, N = 9; +DN-Rac1: n = 19, N = 9), shield (wt: n = 19, N = 12; wt (+Nodal control): n = 12, N = 8; +Nodal: n = 15, N = 7, +Nodal+DN-Rac1: n = 8, N = 3, *control* MO: n = 14, N = 7, *e-cad* MO: n = 20, N = 6) or 75% epiboly stage (wt: n = 9, N = 8; +Nodal: n = 12, N = 6), as a function of their initial sphericity. The average is shown in (j) and individual transplants in (j'). Data are shown as mean ± SEM. Kruskal-Wallis test. NS: not significant. **$P = 0.0078$ (b). Mann-Whitney test (two-sided). ****$P < 0.0001$ (d). NS: not significant (h) (d, h). t test (two-sided). **$P = 0013$ (f). Top view (projection: (a, e), cross-section: (c)). Dorsal view (cross-section: (g)). Scale bar: 20 µm (a, c, e, g).

a
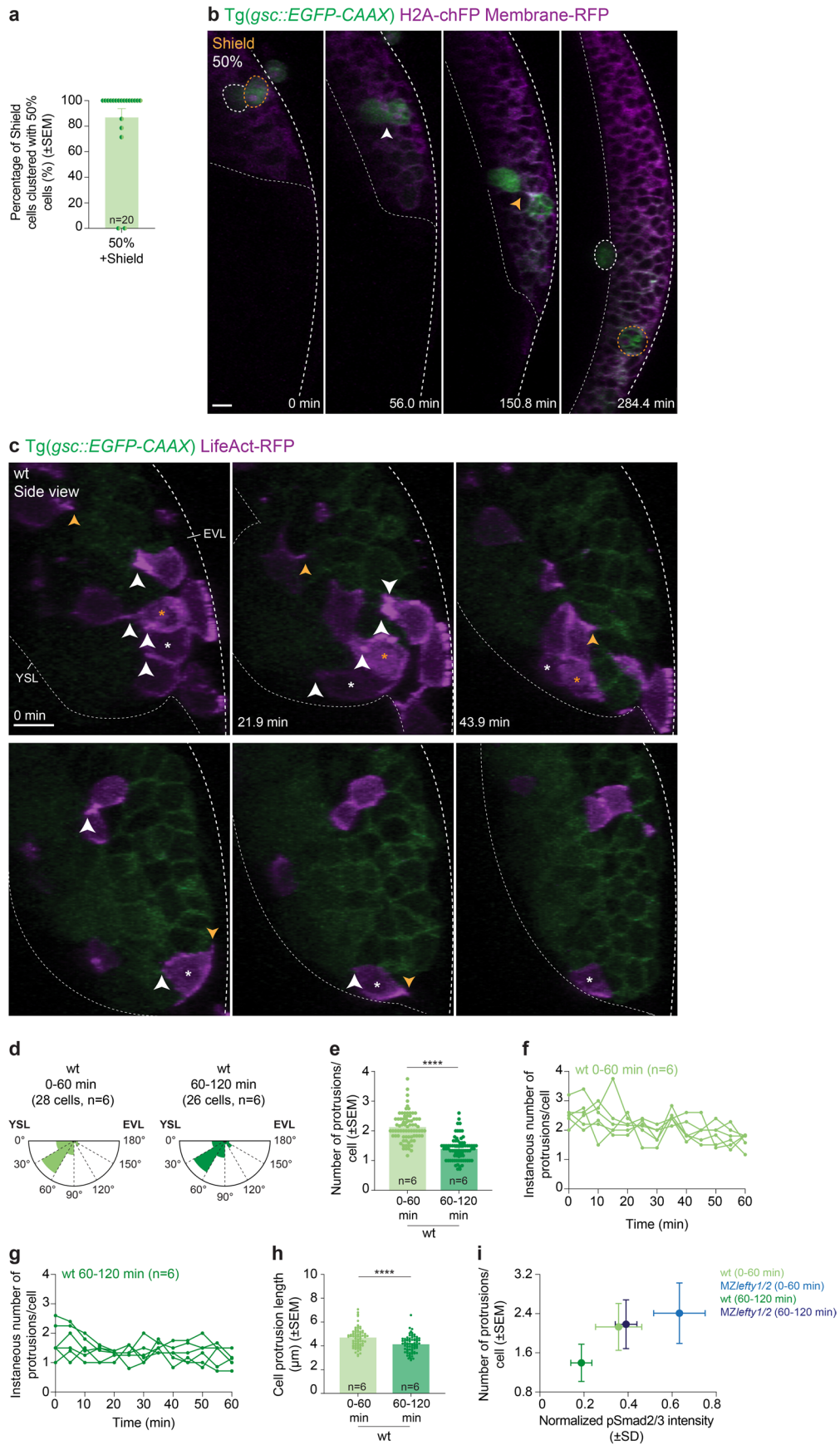
b Tg(*gsc::EGFP-CAAX*) H2A-chFP Membrane-RFP

c Tg(*gsc::EGFP-CAAX*) LifeAct-RFP

d **e** **f** **g** **h** **i**

Extended Data Fig. 6 | See next page for caption.

Extended Data Fig. 6 | Contact between leaders and followers is required for follower cell internalization and in vivo analysis of mesendoderm cell protrusiveness. (a) Percentage of co-transplanted mesendoderm donor cells, collected from 50% epiboly and shield stage embryos, which remain clustered until the end of host embryo epiboly (N = 11). **(b)** High-resolution confocal images of co-transplanted mesendoderm donor cells, collected from 50% epiboly (white lines) and shield (yellow lines) stage embryos. All donor cells express *gsc::EGFP-CAAX* (green) and can be distinguished by H2A-chFP expression (magenta, nuclei). MZ*oep* host express low levels of *gsc::EGFP-CAAX* (green) and Membrane-RFP (magenta). Dashed white lines indicate EVL and YSL. White arrowhead points at an initially cohesive heterotypic cluster. Yellow arrowhead indicates the separation of a heterotypic cluster, with early cells (50%) undergoing internalization and late cells (shield) remaining in more superficial regions of the blastoderm (n = 2/20, N = 10). **(c)** High-resolution confocal images of a wt embryo during mesendoderm internalization. Axial mesendoderm is marked by *gsc::EGFP-CAAX* expression (green) and actin-rich protrusions are mosaically-labelled by LifeAct-RFP (magenta). Dashed white lines as in (b). Arrowheads indicate cell protrusions oriented towards the YSL (white) or EVL (yellow). Asterisks indicate internalizing cells, with the cell located closest to the blastoderm margin initiating internalization first

(white asterisks). 0 min, internalization onset. **(d)** Rose plot of cell protrusion orientation in wt mesendoderm cells internalizing early (0–60 min: N = 6) and late (60–120 min: N = 6; see Methods). **(e)** Average number of protrusions formed by wt mesendoderm cells internalizing early (0–60 min: 28 cells, N = 6) and late (60–120 min: 26 cells, N = 6; see Methods). Each dot corresponds to the average number of protrusions/internalizing mesendoderm cell in a single embryo at a given time point. **(f, g)** Instantaneous number of protrusions formed per wt mesendoderm cell internalizing early (f, 0–60 min: 28 cells, N = 6) or late (g, 0–120 min: 26 cells, N = 6, see Methods). Each curve corresponds to the average number of protrusions/internalizing mesendoderm cell in a single embryo. **(h)** Length of protrusions formed by wt mesendoderm cells internalizing early (0–60 min: 28 cells, N = 6) or late (60–120 min: 26 cells, N = 6; see Methods). Each dot corresponds to the average length of cell protrusions/internalizing mesendoderm cells in a single embryo at a given time point. **(i)** Average number of protrusions formed by wt or MZ*lefty1/2* mesendoderm cells as a function of their normalized pSmad2/3 nuclear accumulation averaged over the first 3 cell tiers (data are also shown in Figs. 2d, 4e, Extended Data Fig. 8b, j and in (e)). Data are shown as mean ± SEM (a, e, h) or SD (i). Mann-Whitney test (two-sided). ****$P < 0.0001$ (e, h). Dorsal view (cross-section: (b, c)). Scale bar: 20 µm (b, c).
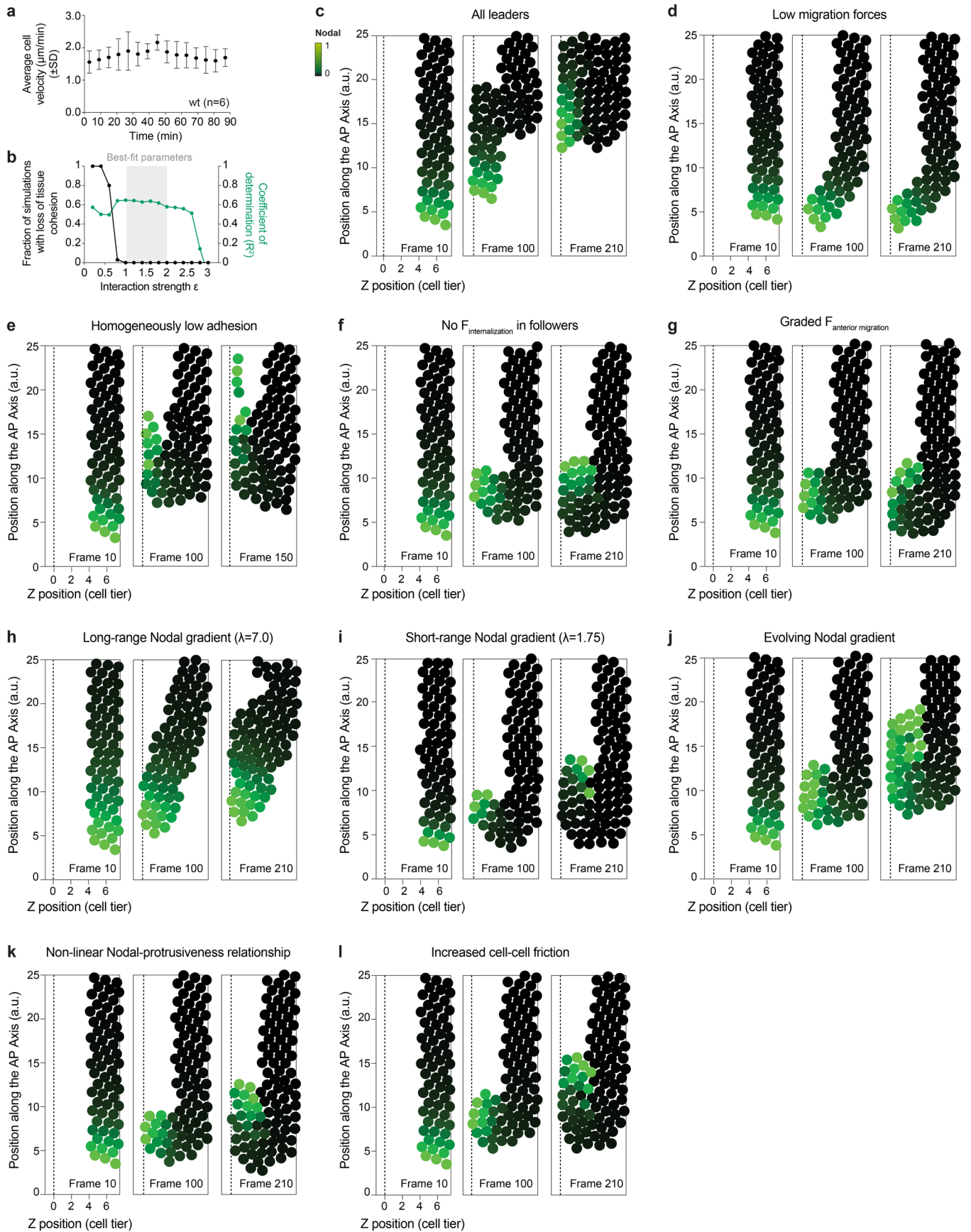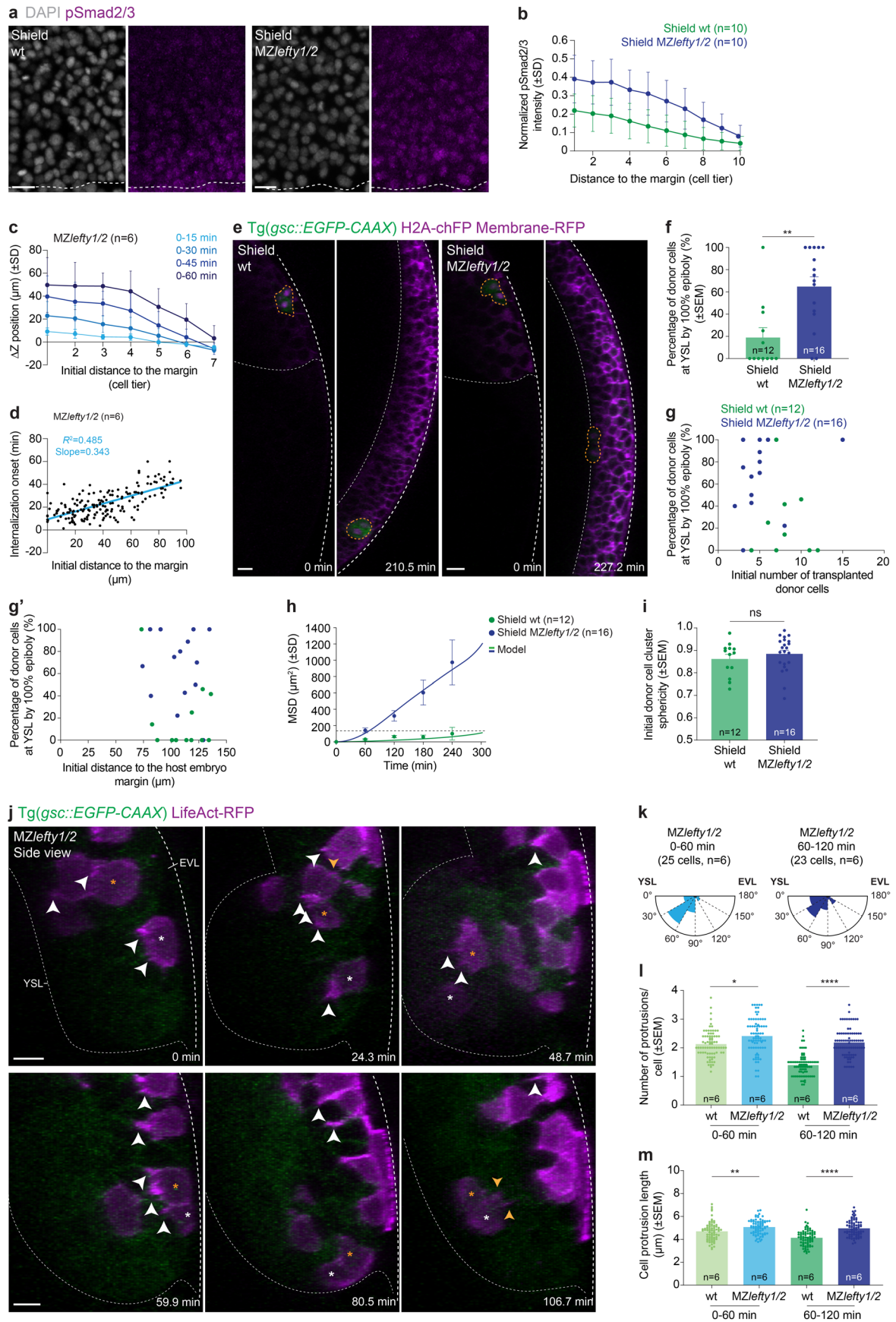
Extended Data Fig. 7 | See next page for caption.

Extended Data Fig. 7 | Sensitivity analysis of the numerical simulations.
(a) Mesendoderm cell velocity, averaged across all wt embryos (N = 6), during epiboly, internalization and anterior migration movements. 0 min, internalization onset. **(b)** Sensitivity analysis for different values of interaction strength ε and its impact on mesendoderm tissue cohesion and preservation of positional order in the numerical simulations. Shaded box indicates the range of best-fit parameters (ensuring both tissue cohesion and high R^2) used in the simulations. **(c-l)** Numerical simulations of mesendoderm internalization for different assumptions (see Supplementary Note). Particles are colour-coded for Nodal signalling activity along the anterior-posterior (AP) axis. Dashed lines indicate the YSL. Mesendoderm cells are defined as any cell with a Nodal signalling >0.05. In (c), all mesendoderm cells, regardless of their Nodal signalling activity, were assumed to have equally high internalization forces. In this case, positional information during tissue internalization was lost, since mesendoderm cells located far from the margin reach the YSL boundary at the same time as cells positioned right at the margin. In (d), all parameters are kept unchanged from those in Fig. 4b (simulating the wt situation), except that lower migratory forces were assumed (both for internalization and animal migration forces). This resulted in a lack of large-scale internalization movements at the margin, as migratory forces were insufficient to drive the cellular rearrangements necessary for morphogenesis. In (e), all parameters are kept unchanged from those in Fig. 4b, except that homogeneously lower adhesion between cells was assumed. This led to loss of tissue-level cohesion during internalization movements, suggesting that a minimum level of cell-cell adhesion is required for tissue integrity during internalization. In (f), all parameters are kept unchanged from those in Fig. 4b, except that zero internalization forces were assumed for all follower cells (defined as any cell with a Nodal signalling

<0.5). In this case, internalization is similar to the situation shown in Fig. 4b, suggesting that the internalization forces of follower cells are largely dispensable to reproduce wt tissue internalization. In (g), all parameters are kept unchanged from those in Fig. 4b, except that the anterior migration-directed forces were also assumed to be proportional to Nodal signalling activity. While the overall tissue movements were, as expected, delayed compared to those in Fig. 4b, it still gave rise to ordered tissue internalization movement. In (h), all parameters are kept unchanged from those in Fig. 4b, except that an expanded Nodal gradient was assumed. Similar to the phenotype of MZ*lefty1/2* embryos (Fig. 4g-j, Extended Data Fig. 8c, d and Supplementary Video 6), this led to the near-simultaneous internalization of many cells at the margin, thus resulting in loss of positional information. In (i), all kept parameters are unchanged from those in Fig. 4b, except that a shorter Nodal gradient was assumed. This led to a smaller population of leader cells, which, nonetheless, was able to initiate robust and orderly tissue internalization. In (j), all parameters are kept unchanged from those in Fig. 4b, except that an evolving Nodal gradient was assumed, whereby cells closest to the margin continue to increase Nodal signalling activity over time. This accelerates the process of internalization and anterior movements, while ordering is largely unchanged. In (k), all parameters are kept unchanged from those in Fig. 4b, except that a cubic, rather than linear, relationship between cell protrusiveness and Nodal signalling activity was assumed. This led to a smaller population of leader cells, which, nonetheless, initiated robust and orderly tissue internalization. In (l), all parameters are kept unchanged from those in Fig. 4b, except that a higher value for cell-cell friction was assumed. In this case, the overall tissue movements were delayed compared to those in Fig. 4b, while positional order remained largely unchanged. Data are shown as mean ± SD.

Extended Data Fig. 8 | See next page for caption.

Extended Data Fig. 8 | Expanding the Nodal signalling gradient affects the spatiotemporal pattern of leader-to-follower cells. (a) High-resolution confocal images of wt and MZ*lefty1/2* embryos stained for DAPI (grey, nuclei) and pSmad2/3 (magenta) at shield stage. Dashed lines indicate deep cell margin. **(b)** Normalized intensity of nuclear pSmad2/3 as a function of their distance to the blastoderm margin in wt and MZ*lefty1/2* embryos at shield stage (N = 3). **(c)** Change in Z position, a proxy for cell internalization, of mesendoderm cells as a function of their initial distance to the margin in MZ*lefty1/2* embryos (N = 6). Colour-code corresponds to distinct time bins. **(d)** Onset of mesendoderm cell internalization as a function of the initial distance to the blastoderm margin in MZ*lefty1/2* embryos (N = 6). **(e)** High-resolution confocal images of transplanted wt and MZ*lefty1/2* donor cells, collected from shield stage embryos. Donor cells are marked by *gsc::EGFP-CAAX* (green) and H2A-chFP expression (magenta, nuclei). MZ*oep* hosts express low levels of *gsc::EGFP-CAAX* (green) and Membrane-RFP (magenta). For each transplant, the first acquired time point and the time point when the hosts reached 100% epiboly are shown. Dashed white lines indicate EVL and YSL. Yellow dashed lines outline donor cell transplants. **(f)** Percentage of internalized control (N = 7) and MZ*lefty1/2* (N = 6) mesendoderm donor cells, collected from shield stage embryos, by the end of host embryo epiboly. **(g, g')** Percentage of internalized control (N = 7) and MZ*lefty1/2* (N = 6) mesendoderm donor cells, collected from shield stage embryos, as a function of the initial number of transplanted cells (f) or the initial distance of the transplanted cells to the host embryo margin (f'). **(h)** Mean squared relative displacement (MSD) of transplanted donor mesendoderm cells, collected from wt (N = 7) or MZ*lefty1/2* (N = 6) embryos at shield stage, and predicted by the model based on their measured average protrusiveness (see (l)). Dashed line corresponds to the average cell size at 300 min (see also (f) for

the percentage of internalized cells for these transplants and Supplementary Note). **(i)** Initial sphericity of transplanted control (N = 7) and MZ*lefty1/2* (N = 6) mesendoderm donor cell clusters, collected from shield stage embryos. **(j)** High-resolution confocal images of mesendoderm internalization in a MZ*lefty1/2* embryo. Axial mesendoderm is marked by *gsc::EGFP-CAAX* expression (green), while actin-rich protrusions are mosaically-labelled by LifeAct-RFP (magenta). Dashed lines as in (d). Arrowheads indicate cell protrusions oriented towards the YSL (white) or EVL (yellow). Asterisks indicate internalizing cells. 0 min, internalization onset. In contrast to wt embryos, mesendoderm cells in MZ*lefty1/2* embryos positioned closer or further away from the blastoderm margin initiate internalization movements almost simultaneously, resulting in loss of positional information (compare white and orange asterisks). **(k)** Rose plot of cell protrusion orientation in mesendoderm cells internalizing early (0–60 min: N = 6) and late (60–120 min: N = 6; see Methods) in MZ*lefty1/2* embryos. **(l)** Average number of protrusions formed by mesendoderm cells internalizing early (0–60 min) and late (60–120 min) in wt (28 and 26 cells, N = 6) or MZ*lefty1/2* (25 and 23 cells, N = 6) embryos (see Methods). Each dot corresponds to the average number of protrusions/internalizing cell in a single embryo at a given time point. **(m)** Length of protrusions formed by mesendoderm cells internalizing early (0–60) and later (60–120 min) in wt (28 and 26 cells, N = 6) or MZ*lefty1/2* (25 and 23 cells, N = 6) embryos (see Methods). Each dot corresponds to the average length of cell protrusions/internalizing cell in a single embryo at a given time point. The data shown for wt cells in (j, k) are also shown in Extended Data Fig. 6e and h. Data are shown as mean ± SD (b, c) or SEM (f, i, l, m). Mann-Whitney test (two-sided). **P = 0.0027 (f). t test (two-sided). NS: Not significant (i). Kruskal-Wallis test. *P = 0.0343 (l). **P = 0.0022 (m). ****P < 0.0001 (l, m). Dorsal view (top view: (a); cross-section: (e, j)). Scale bars: 20 μm (a, e, j).
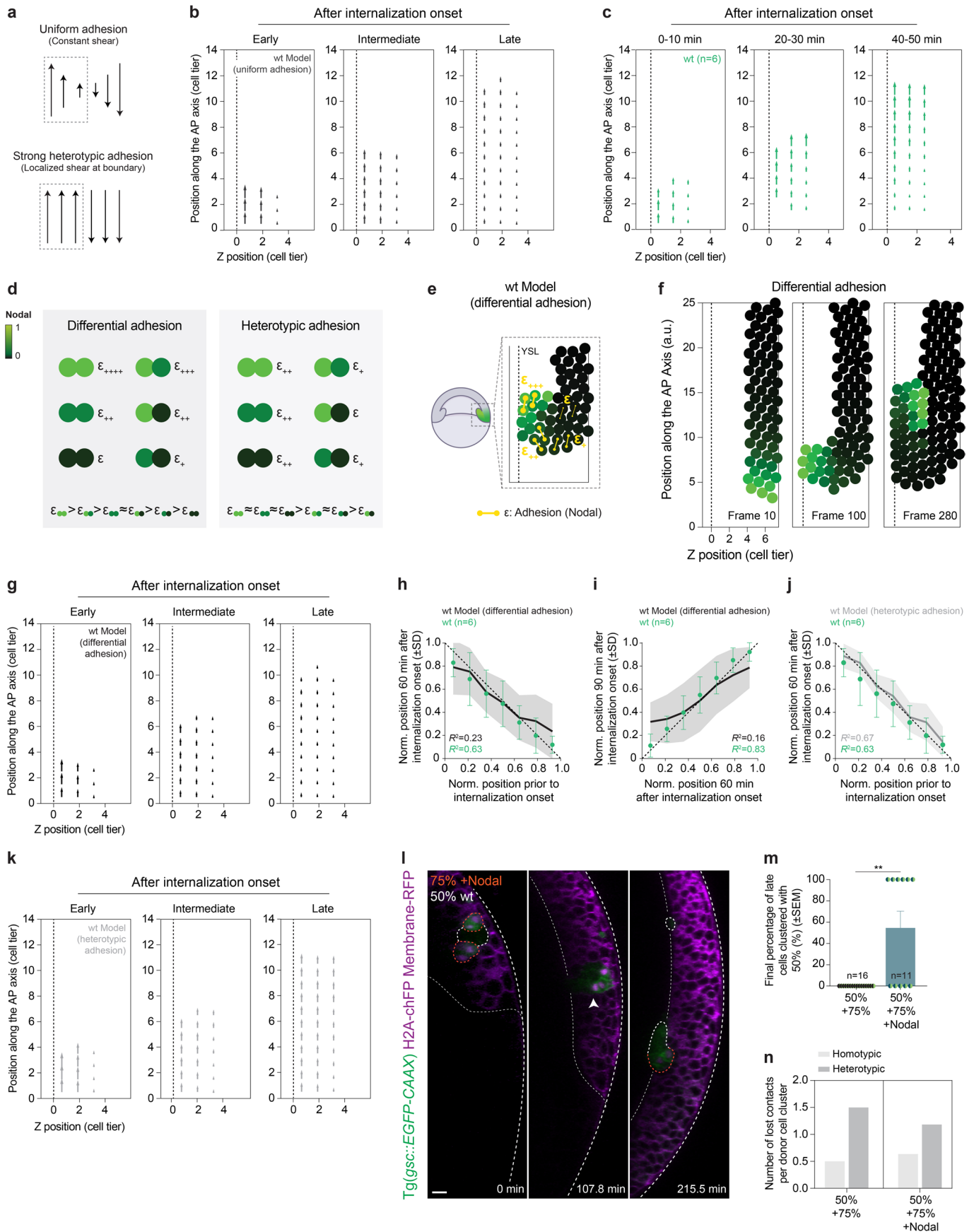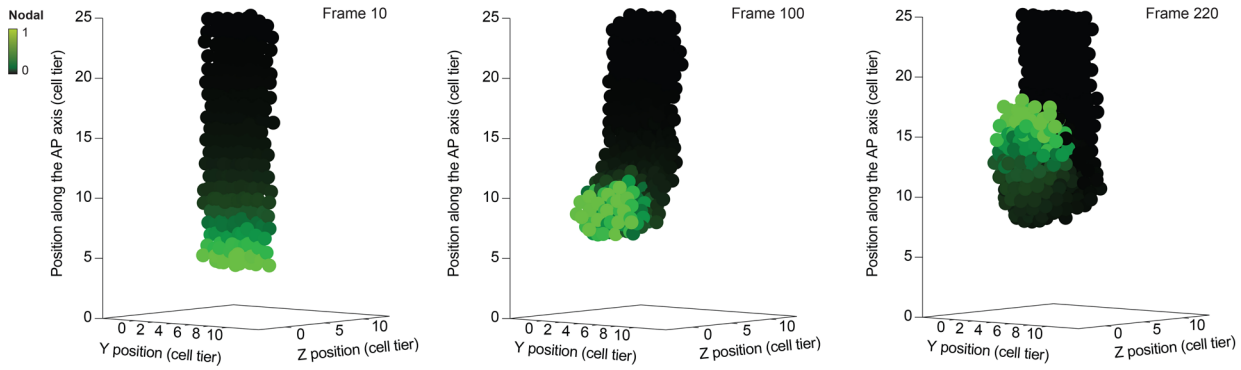
Extended Data Fig. 9 | See next page for caption.

Extended Data Fig. 9 | Modulating Nodal signalling in heterotypic clusters of transplanted mesendoderm cells is sufficient to rescue cluster splitting.
**(a)** Schematic representation of the velocity gradients expected to arise at the boundary between internalized and non-internalized cells (grey box) in the simulations for different model assumptions. For uniform cell-cell interactions, velocity gradients are expected to be constant, as observed in shearing of simple fluids (near-zero velocities arise at the boundary). For strongly heterotypic adhesion, velocity gradients are expected to be concentrated at the boundary (where interactions are weak), with near-constant velocities on either side. **(b)** Average velocity maps of internalized mesendoderm cells during anterior migration in wt simulations assuming uniform adhesion (see Supplementary Note). The maps were 'stage-matched' to the average position of internalized mesendoderm cells along the anterior-posterior (AP) axis in vivo (early, intermediate and late correspond to frames 80, 130, 250, respectively). Dashed lines indicate the YSL. **(c)** Average velocity maps of internalized mesendoderm cells during anterior migration in wt embryos (N = 6, see Supplementary Note). Dashed line as in (b). **(d)** Schematic representation of the Nodal signalling-dependent differential and heterotypic/preferential adhesion models and their implications for the strength of contacts between cells with different Nodal signalling activity. Particles are colour-coded for Nodal signalling activity. **(e)** Schematic representation of the 2D-particle based model assuming Nodal signalling-dependent differential adhesion (see Supplementary Note). All remaining parameters as in Fig. 4b. Colour-code as in (d) and dashed line as in (b). **(f)** Numerical simulations using the same parameters as in Fig. 4b, except that Nodal signalling-dependent differential adhesion was assumed (see Supplementary Note). Colour-code as in (d) and dashed lines as in (b). Similar to our simulations assuming uniform adhesion, in these simulations, leader cells are highly adhesive and, therefore, interact strongly with the overlying non-internalized cells, resulting in loss of positional information. **(g)** Average velocity maps of internalized mesendoderm cells during anterior migration in wt simulations assuming Nodal signalling-dependent differential adhesion (see Supplementary Note). The maps were 'stage-matched' to the average position of internalized mesendoderm cells along the AP axis in vivo (early, intermediate and late correspond to frames 100, 150, 280, respectively). Dashed lines as in (b). **(h, i)** Correlation between cell position at early (h) and late (i) stages of tissue internalization in wt simulations assuming Nodal signalling-dependent differential adhesion ($R^2 = 0.23$ (h), $R^2 = 0.16$ (i)) and wt embryos ($R^2 = 0.63$ (h), $R^2 = 0.83$ (i)), N = 6; see Supplementary Note). Dashed line indicates perfect conservation of the relative cell position during internalization ($R^2 = 1$). **(j)** Correlation between cell position at the onset of tissue internalization in wt simulations assuming Nodal signalling-dependent heterotypic adhesion ($R^2 = 0.67$) and wt embryos ($R^2 = 0.63$, N = 6; see Supplementary Note). Dashed line as in (h, i). **(k)** Average velocity maps of internalized cells during anterior migration in wt simulations assuming Nodal signalling-dependent heterotypic interactions (see Supplementary Note). The maps were 'stage-matched' to the average position of internalized mesendoderm cells along the AP axis in vivo (early, intermediate and late correspond to frames 70, 120, 210, respectively). Dashed lines as in (b). **(l)** High-resolution confocal images of a heterotypic cluster of co-transplanted mesendoderm cells, collected from wt embryos at 50% and Nodal-overexpressing embryos at 75% epiboly stage. All donor cells express *gsc::EGFP-CAAX* (green) and can be distinguished by H2A-chFP expression (magenta, nuclei). MZ*oep* hosts express low levels of *gsc::EGFP-CAAX* (green) and Membrane-RFP (magenta). Dashed white lines indicate the EVL and YSL. Thick white lines and orange dashed lines outline donor cells collected from wt embryos at 50% epiboly and Nodal-overexpressing embryos at 75% epiboly stage, respectively. White arrowhead points at a cohesive heterotypic cluster. **(m)** Percentage of co-transplanted control (N = 9) or Nodal-overexpressing (N = 7) donor cells collected from 75% epiboly stage embryos, which remain clustered with early cells (50% epiboly) until the end of host epiboly. **(n)** Number of homotypic or heterotypic contacts lost upon the final splitting of mesendoderm donor cell clusters of different compositions (see (m) for n and N), normalized to the number of transplanted clusters. The data shown for heterotypic clusters composed of 50% and 75% epiboly in (m, n) are also shown in Fig. 5g, h. Data are shown as mean ± SD (h-j) or SEM (m). Mann-Whitney test (two-sided). **$**P = 0.0016$ (m). Dorsal view (cross-section: (l)). Scale bar: 20 µm (l).
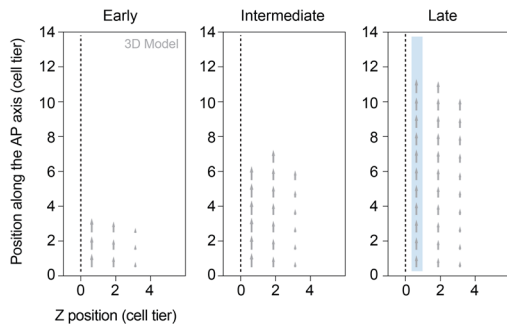
a 3D simulations

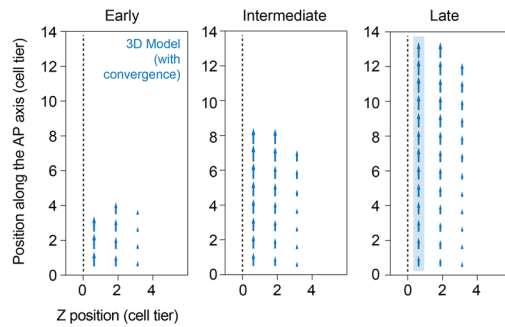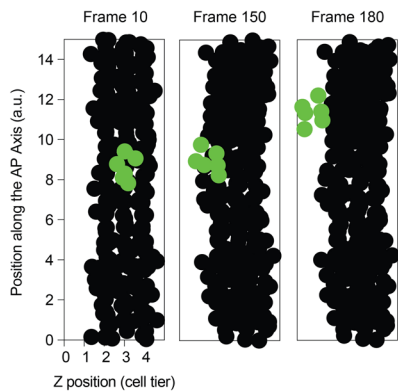**b 3D simulations with convergence forces**
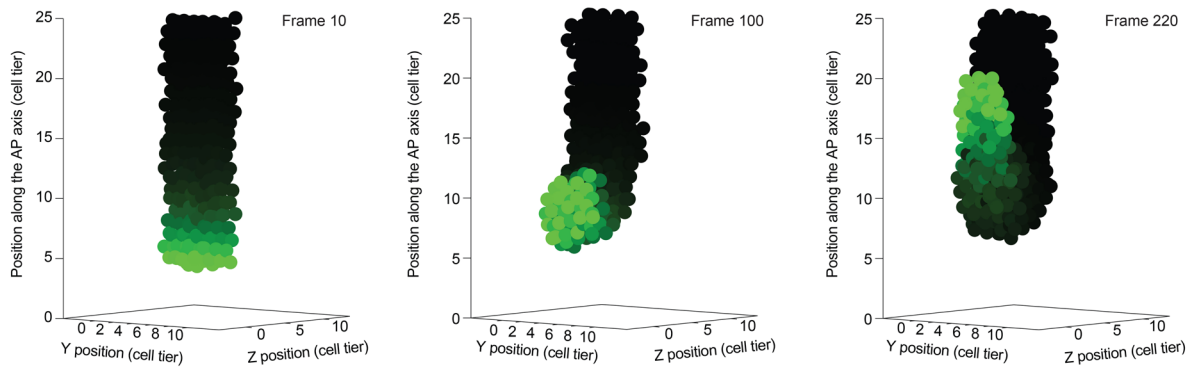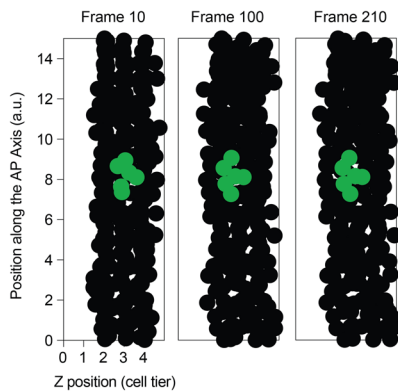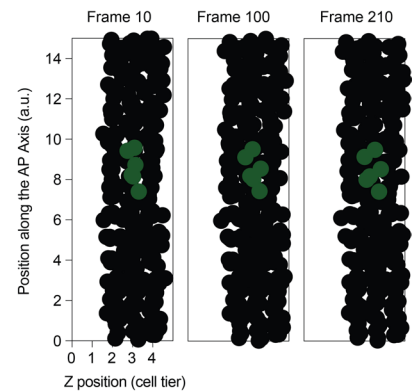
Extended Data Fig. 10 | See next page for caption.

Extended Data Fig. 10 | 3D simulations of mesendoderm internalization in vivo and in transplantation assays. (a, b) 3D numerical simulations of mesendoderm cell internalization with or without convergence forces (see Supplementary Note). Particles are colour-coded for Nodal signalling activity. Mesendoderm cells are defined as any cell with a Nodal signalling >0.05. AP: anterior-posterior axis. In (a), all parameters are kept unchanged from those in Fig. 5d (simulating the wt situation with heterotypic adhesion), except that 7 adjacent cell rows, rather than a single 2D cross-section, were simulated. These 3D simulations produced similarly ordered and robust mesendoderm internalization as observed in the 2D model. In (b), additional convergence forces in the Y-direction were added. While this produced convergence-extension movements within the tissue, it still led to similarly ordered and robust mesendoderm internalization as observed in the 2D model. **(c, d)** Average velocity maps of internalized cells during anterior migration in 3D simulations with or without convergence forces (see Supplementary Note). The maps were 'stage-matched' to the average position of internalized mesendoderm cells along the AP axis in vivo (early, intermediate and late in these simulations correspond to frames 100, 160, 220, respectively). Dashed lines indicate the YSL. While convergence forces did not affect the velocity gradients found along the Z direction (with all internalized mesendoderm cells migrating at similar speeds at a distance from the margin), it did create an additional velocity gradient along the AP axis (shaded blue boxes). This arises due to bidirectional extension movements and is reminiscent of the velocity maps in vivo (see also 50 min in Extended Data Fig. 9c). **(e-g)** 3D numerical simulations of mesendoderm cell internalization in transplantation assays, for different values of Nodal activity in the transplanted cells (N = 1.0 in (e), N = 0.666 in (f), N = 0.333 in (g), see Supplementary Note). The simulations were initialized with cohesive transplants composed of 6 cells and, consistent with previous findings[41], MZ*oep* hosts were assumed to have negligibly low Nodal signalling. As expected from our toy-model of motility-driven (un)jamming, for sufficiently large Nodal signalling activity (and thus protrusive forces), transplanted cells were able to internalize and subsequently migrate towards the animal pole of the embryo (e). For intermediate to low Nodal signalling activity in the transplanted cells, the simulated clusters remained jammed within the host tissue and fail to undergo internalization (f, g).

nature portfolio

Corresponding author(s): Edouard Hannezo and Carl-Philipp Heisenberg

Last updated by author(s): 23-08-2022

Reporting Summary

Nature Portfolio wishes to improve the reproducibility of the work that we publish. This form provides structure for consistency and transparency in reporting. For further information on Nature Portfolio policies, see our Editorial Policies and the Editorial Policy Checklist.

Statistics

For all statistical analyses, confirm that the following items are present in the figure legend, table legend, main text, or Methods section.

n/a	Confirmed	
☐	☒	The exact sample size (*n*) for each experimental group/condition, given as a discrete number and unit of measurement
☐	☒	A statement on whether measurements were taken from distinct samples or whether the same sample was measured repeatedly
☐	☒	The statistical test(s) used AND whether they are one- or two-sided *Only common tests should be described solely by name; describe more complex techniques in the Methods section.*
☐	☒	A description of all covariates tested
☐	☒	A description of any assumptions or corrections, such as tests of normality and adjustment for multiple comparisons
☐	☒	A full description of the statistical parameters including central tendency (e.g. means) or other basic estimates (e.g. regression coefficient) AND variation (e.g. standard deviation) or associated estimates of uncertainty (e.g. confidence intervals)
☐	☒	For null hypothesis testing, the test statistic (e.g. *F*, *t*, *r*) with confidence intervals, effect sizes, degrees of freedom and *P* value noted *Give P values as exact values whenever suitable.*
☒	☐	For Bayesian analysis, information on the choice of priors and Markov chain Monte Carlo settings
☒	☐	For hierarchical and complex designs, identification of the appropriate level for tests and full reporting of outcomes
☒	☐	Estimates of effect sizes (e.g. Cohen's *d*, Pearson's *r*), indicating how they were calculated

Our web collection on statistics for biologists contains articles on many of the points above.

Software and code

Policy information about availability of computer code

Data collection	Image visualization was performed using Fiji (NIH) and/or Bitplane Imaris.
Data analysis	All image data analysis was performed using Fiji (NIH) and/or Bitplane Imaris. The data analysis, statistics and plots were generated using Microsoft Excel, Gnuplot and/or GraphPad Prism. To analyze the cell transplantations assays and the nuclear accumulation of Smad2/3 we used a Matlab custom-made code from a previous publication, which is already publicly avaliable in the original reference (Schauer, et al. elife. 2020). The code for the simulations of mesendoderm internalization is provided as a Supplementary File.

For manuscripts utilizing custom algorithms or software that are central to the research but not yet described in published literature, software must be made available to editors and reviewers. We strongly encourage code deposition in a community repository (e.g. GitHub). See the Nature Portfolio guidelines for submitting code & software for further information.

Data

Policy information about availability of data

All manuscripts must include a data availability statement. This statement should provide the following information, where applicable:
- Accession codes, unique identifiers, or web links for publicly available datasets
- A description of any restrictions on data availability
- For clinical datasets or third party data, please ensure that the statement adheres to our policy

All data that support the findings of this study are available from the corresponding author upon reasonable request (a statement to this effect was added in the Methods section).

Field-specific reporting

Please select the one below that is the best fit for your research. If you are not sure, read the appropriate sections before making your selection.

☒ Life sciences ☐ Behavioural & social sciences ☐ Ecological, evolutionary & environmental sciences

For a reference copy of the document with all sections, see nature.com/documents/nr-reporting-summary-flat.pdf

Life sciences study design

All studies must disclose on these points even when the disclosure is negative.

Sample size	All sample sizes and independent replicates are indicated in the figure legends and the criteria used to classify independent replicates is indicated in the Statistics session of the Methods.
Data exclusions	All criteria used to exclude data are indicated in the corresponding section of the Methods section.
Replication	All experiments described in the manuscript were repeated at least 3 independent times, except for the in situ hybridizations with the sox17 probe which were only repeated twice (this information is specified in the corresponding figure legend and again in the Statistics session of the Methods).
Randomization	The allocation of samples was random.
Blinding	No blinding was performed either in data collection nor in data analysis.

Reporting for specific materials, systems and methods

We require information from authors about some types of materials, experimental systems and methods used in many studies. Here, indicate whether each material, system or method listed is relevant to your study. If you are not sure if a list item applies to your research, read the appropriate section before selecting a response.

Materials & experimental systems

n/a	Involved in the study
☐	☒ Antibodies
☒	☐ Eukaryotic cell lines
☒	☐ Palaeontology and archaeology
☐	☒ Animals and other organisms
☒	☐ Human research participants
☒	☐ Clinical data
☒	☐ Dual use research of concern

Methods

n/a	Involved in the study
☒	☐ ChIP-seq
☒	☐ Flow cytometry
☒	☐ MRI-based neuroimaging

Antibodies

Antibodies used	The antibodies used in this study are detailed in the Methods section (sections: "Whole-mount immunofluorescence (WMIF)" and "Whole-mount in situ hybridization") along with information of the supplier, catalog number, clone number and lot number. Briefly, we used: α-pSmad2/3 (Cell signalling, Clone D27F4, Cat#:8828), α-E-Cadherin (rabbit anti-zebrafish E-Cadherin, published in Maitre et al. 2012), Alexa Fluor 546 Goat Anti-rabbit IgG (Thermo Fisher Scientific, Cat#:A-11010) and Anti-Digoxigenin-AP Fab fragments (Roche, Cat#11093274910).
Validation	These antibodies are commercially available and have been extensively used in previous publications, also provided in the manuscript. Here are their corresponding RRID: α-pSmad2/3 (RRID:AB_2631089), α-E-Cadherin (rabbit anti-zebrafish E-Cadherin, published in Maitre et al. 2012), Alexa Fluor 546 Goat Anti-rabbit IgG (RRID:AB_2534077) and Anti-Digoxigenin-AP Fab fragments (RRID:AB_2734716).

Animals and other organisms

Policy information about studies involving animals; ARRIVE guidelines recommended for reporting animal research

Laboratory animals	Zebrafish (Danio rerio) - all strains are detailed, along with the corresponding references, in the "Fish lines and husbandry" section of the Methods.
Wild animals	n/a
Field-collected samples	n/a

Ethics oversight | All animal breeding and procedures were performed in accordance with the European Union animal welfare guidelines and involved only low severity lines, in accordance with the authorized animal breeding license (66018/8-II/3b/2013). All experiments were performed before 5 days post-fertilization, a period during which zebrafish do not feed independently and in line with the 3R's principles.

Note that full information on the approval of the study protocol must also be provided in the manuscript.